



Third Radiation Transfer Model Intercomparison (RAMI) exercise: Documenting progress in canopy reflectance models

Jean-Luc Widlowski, Malcolm Taberner, Bernard Pinty, Véronique Bruniquel-Pinel, Mathias Disney, Richard Fernandes, Jean-Philippe Gastellu-Etchegorry, Nadine Gobron, Andres Kuusk, Thomas Lavergne, et al.

► To cite this version:

Jean-Luc Widlowski, Malcolm Taberner, Bernard Pinty, Véronique Bruniquel-Pinel, Mathias Disney, et al.. Third Radiation Transfer Model Intercomparison (RAMI) exercise: Documenting progress in canopy reflectance models. *Journal of Geophysical Research*, American Geophysical Union, 2007, 112 (D9), pp.D09111:1-28. <10.1029/2006JD007821>. <ird-00405091>

HAL Id: ird-00405091
<http://hal.ird.fr/ird-00405091>

Submitted on 20 Jul 2009

HAL is a multi-disciplinary open access archive for the deposit and dissemination of scientific research documents, whether they are published or not. The documents may come from teaching and research institutions in France or abroad, or from public or private research centers.

L'archive ouverte pluridisciplinaire **HAL**, est destinée au dépôt et à la diffusion de documents scientifiques de niveau recherche, publiés ou non, émanant des établissements d'enseignement et de recherche français ou étrangers, des laboratoires publics ou privés.

1 The third RADIATION transfer Model Intercomparison (RAMI) 2 exercise: Documenting progress in canopy reflectance models

J-L. Widlowski,¹ M. Taberner,¹ B. Pinty,¹ V. Bruniqnel-Pinel,² M. Disney,³ R. Fernandes,⁴ J-P. Gastellu-Etchegorry,⁵ N. Gobron,¹ A. Kuusk,⁶ T. Lavergne,¹ S. Leblanc,⁷ P. E. Lewis,³ E. Martin,⁵ M. Möttus,⁶ P. R. J. North,⁸ W. Qin,⁹ M. Robustelli,¹ N. Rochdi,⁴ R. Ruiloba,² C. Soler,¹⁰ R. Thompson,¹¹ W. Verhoef,¹² M. M. Verstraete,¹ D. Xie,¹³

3 Abstract.

4 The RADIATION transfer Model Intercomparison (RAMI) initiative benchmarks canopy
5 reflectance models under well-controlled experimental conditions. Launched for the first
6 time in 1999 this triennial community exercise encourages the systematic evaluation of
7 canopy reflectance models on a voluntary basis. The first phase of RAMI focused on doc-
8 umenting the spread among radiative transfer (RT) simulations over a small set of pri-
9 marily 1-D canopies. The second phase expanded the scope to include structurally com-
10 plex 3-D plant architectures with and without background topography. Here sometimes
11 significant discrepancies were noted which effectively prevented the definition of a reli-
12 able “surrogate truth” – over heterogeneous vegetation canopies – against which other
13 RT models could then be compared. The present paper documents the outcome of the
14 third phase of RAMI, highlighting both the significant progress that has been made in
15 terms of model agreement since RAMI-2, and the capability of/need for RT models to
16 accurately reproduce local estimates of radiative quantities under conditions that are rem-
17 iniscent of *in situ* measurements. Our assessment of the self-consistency, the relative- and
18 absolute performance of 3-D Monte Carlo models in RAMI-3 supports their usage in the
19 generation of a “surrogate truth” for all RAMI test cases. This development then leads
20 1) to the presentation of the ‘RAMI On-line Model Checker’ (ROMC), an open-access
21 web-based interface to evaluate RT models automatically, and 2) to a reassessment of
22 the role, scope and opportunities of the RAMI project in the future.

1. Introduction

23 Space-borne observations constitute a highly appropri-
24 ate source of information to quantify and monitor earth
25 surface processes. The quality/confidence that may be
26 associated with the outcome of interpretation and assim-
27 ilation efforts of these data streams, however, relies heav-
28 ily on the actual performance of the available modelling
29 tools. This understanding has led to a series of model
30 intercomparison projects (MIP) aiming either to docu-
31 ment the spread of currently available simulation mod-
32 els, or, else to assess and benchmark the quality of their
33 simulation results, *e.g.*, *Henderson-Sellers et al.* [1995];
34 *Gates et al.* [1998]; *Dirmeyer et al.* [1999]; *Pinty et al.*
35 [2001]; *Latif et al.* [2001]; *Cahalan et al.* [2005]; *Ran-*
36 *gasayi et al.* [2005]. Among these MIPs the RADIATION
37 transfer Model Intercomparison (RAMI) activity focuses
38 on the proper representation of the radiative processes
39 occurring, in vegetated environments, in the optical do-
40 main of the solar spectrum. The design and launch of
41 the first phase of RAMI occurred approximately in par-
42 allel with that of the ‘Intercomparison of 3-D Radiation
43 Codes’ (I3RC) activity which deals with the correct rep-
44 resentation of the radiative properties of 3-D cloud fields
45 (<http://i3rc.gsfc.nasa.gov/>). Both MIPs collaborate
46 actively and share their evaluation methodologies in or-
47 der to overcome the difficulties associated with model

¹European Commission, DG Joint Research Centre,

48 benchmarking in the absence of absolute reference stan-
49 dards.

50

51 The first phase of RAMI (RAMI-1) was launched in
52 1999. Its prime objective was to document the variabil-
53 ity that existed between canopy reflectance models when
54 run under well controlled experimental conditions [*Pinty*
55 *et al.*, 2001]. The positive response of the various RAMI-
56 1 participants and the subsequent improvements made
57 to a series of radiative transfer (RT) models promoted
58 the launching of the second phase of RAMI (RAMI-2)
59 in 2002. Here the number of test cases was expanded
60 to focus further on the performance of models dealing
61 with structurally complex 3-D plant environments. The
62 main outcomes of RAMI-2 included 1) an increase in the
63 number of participating models, 2) a better agreement
64 between the model simulations in the case of the struc-
65 turally simple scenes inherited from RAMI-1, and 3) the
66 need to reduce the sometimes substantial differences be-
67 tween some of the 3-D RT models over complex hetero-
68 geneous scenes [*Pinty et al.*, 2004b]. The latter issue
69 was noted as one of the challenges that future intercom-
70 parison activities would have to face, since the reliable
71 derivation of some sort of “surrogate truth” data set will
72 not be possible in the absence of any agreement between
73 these RT models. This, in turn, would then imply that—
74 except in some simple special cases—the evaluation of RT
75 model simulations can not proceed beyond their mutual
76 comparison due to the general lack of absolute reference
77 standards.

78

79 This paper will describe the outcome of the third phase
80 of RAMI (RAMI-3). Section 2 will provide an overview
81 of the organisation and model evaluation protocol em-
82 ployed during RAMI-3. Section 3 documents how the
83 performance of RT models—when applied to the various
84 baseline scenarios inherited from RAMI-1—improved be-

Institute for Environment and Sustainability, Global
Environment Monitoring Unit, TP 440, via E. Fermi 1,
I-21020 Ispra (VA), Italy.

²NOVELTIS, Parc Technologique du Canal, 2 avenue de
l’Europe, 31520 Ramonville Saint-Agne, France.

³Department of Geography, University College London,
26 Bedford Way, London, WC1H 0AP, UK, and NERC
Centre for Terrestrial Carbon Dynamics.

⁴Canada Centre for Remote Sensing, Natural Resources
Canada, 588 Booth Str., Ottawa, ONT K1A 0Y7, Canada

⁵Centre d’Etudes Spatiales de la BIOSphère, 18 av.
Edouard Belin, bpi 2801, 31401 Toulouse cedex 9, France

⁶Tartu Observatory, 61602 Tõravere, Estonia.

⁷Centre Spatial John H. Chapman, 6767, Route de
l’Aéroport, Saint-Huber, Québec, Canada, J3Y 8Y9.

⁸Climate and Land-Surface Systems Interaction Centre,
Department of Geography, University of Wales Swansea,
Singleton Park, Swansea, SA2 8PP, UK.

⁹Science Systems and Applications, Inc., Greenbelt,
Maryland, USA.

¹⁰ARTIS, INRIA Rhône-Alpes, 655, Avenue de l’Europe,
38334 Saint Ismier Cedex, France

¹¹Alachua Research Institute, Alachua, Florida, USA.

¹²National Aerospace Laboratory NLR, P.O. Box 153
8300 AD Emmeloord, Netherlands

¹³Research Center for Remote Sensing and GIS, School of
Geography, Beijing Normal University, Xijiekouwai Street
19, Beijing, China.

85 tween RAMI-2 and RAMI-3. Section 4 documents the
86 outcome of model simulations for the newly proposed ex-
87 periments and measurement types in RAMI-3. Section 5
88 summarises the main achievements and issues observed
89 during RAMI-3 and introduces the “Rami On-line Model
90 Checker” (ROMC), a web-based tool intended to auto-
91 mate the process of RT model benchmarking. Section 5
92 also describes possible roadmaps for the future develop-
93 ment of the RAMI initiative.

2. The third phase of RAMI

94 The third phase of RAMI was officially launched at
95 the end of March 2005. Scientists from around the world
96 with an interest in canopy RT modelling were invited to
97 participate in this triennial benchmarking exercise. A
98 dedicated website (<http://rami-benchmark.jrc.it/>)¹
99 provided detailed descriptions regarding the structural,
100 spectral and illumination conditions of the test cases
101 proposed for RAMI-3. Prior to going public, each one
102 of these experiments and measurements had been ap-
103 proved by the RAMI advisory body, a small group of well-
104 known scientists in the field of radiative transfer mod-
105 elling and/or model intercomparison activities. RAMI-
106 3 included and built upon the various experiments and
107 measurements proposed during earlier phases of RAMI
108 (see Section 2.1 in *Pinty et al.* [2001] and Section 2 in
109 *Pinty et al.* [2004b]). Overall, the number of simulation
110 scenarios grew by 37% with respect to RAMI-2, which
111 led to two separate submission deadlines, namely, July
112 30th 2005 for all RT simulations pertaining to struc-
113 turally homogeneous vegetation canopies and December
114 15th 2005 for all those simulations relating to structurally
115 heterogeneous test cases. As was the case during pre-
116 vious phases of RAMI, the collection of the submitted
117 RT model results and their detailed analysis were per-
118 formed at the Joint Research Centre (JRC) of the Eu-
119 ropean Commission in Ispra, Italy. Two public presen-
120 tations describing the outcome of this community effort
121 were delivered, the first one—dealing with homogeneous
122 test cases only—was given during the 9th International
123 Symposium on Physical Measurements and Signatures in
124 Remote Sensing (ISPMSRS) in Beijing, China (October
125 2005), and the second one—including also the heteroge-
126 neous test cases—at the 4th International workshop on
127 multi-angular measurements and models (IWMMM-4) in
128 Sydney, Australia (March 2006).

129
130 Table 1 lists the models that participated in RAMI-
131 3, the main publications describing these models and
132 the names and affiliations of their operators. Also
133 indicated are the corresponding modelling approaches
134 that are used in order to simulate the radiation
135 transfer. These include Monte Carlo (MC) tech-
136 niques associated with forward/reverse ray-tracing meth-
137 ods (*Drat*, *FLIGHT*, *frat*, *raytran*, *Rayspread* and
138 *Sprint3*) or radiosity approaches (*RGM* and *Hyemalis*),
139 purely analytical formulations (*2-Stream*), as well
140 as, a large number of hybrid techniques, that com-
141 bine one or more of the above with numerical,
142 stochastic and/or geometric optical approaches (*ACRM*,
143 *DART*, *1/2-discret*, *FRT*, *MAC*, *MBRF*, *Sail++*, *4SAIL2*,
144 *5Scale*). More detailed information on the participat-
145 ing models can be found on the RAMI website under
146 [http://rami-benchmark.jrc.it/HTML/RAMI3/MODELS/M](http://rami-benchmark.jrc.it/HTML/RAMI3/MODELS/MODELS.php)
147 [ODELS.php](http://rami-benchmark.jrc.it/HTML/RAMI3/MODELS/MODELS.php). Most of the participants received substantial
148 feedback on the performance of their model(s) both as
149 a result of phases 1 and 2, and in the case of obvious
150 errors/deviations also during phase 3 of RAMI. Conse-

151 quently, all results presented below refer to the latest and
152 most up-to-date version of these models. It is important
153 that prospective users of these models ensure that they
154 have access to the most recent version of these codes, as
155 the performance information provided here may not be
156 representative of, or applicable to, earlier versions.
157

158 One of the traits of RAMI is to increase the number
159 of test cases by including a few new experiments (and
160 measurements) from one phase to another. This strategy
161 serves a dual purpose, namely, a) to allow the evaluation
162 of RT models under an increasingly comprehensive set of
163 structural, spectral and also illumination conditions, and
164 b) to tailor new sets of RAMI experiments and measure-
165 ments around scientific questions emerging in the context
166 of RT modelling and the quantitative interpretation of
167 remotely sensed data. Indeed, such an approach guar-
168 antees that every phase will contain at least some test
169 cases for which the simulation results cannot be known
170 *a priori*. Within RAMI-3 the following new experiments
171 were proposed: 1) a conservative scattering scenario for
172 the heterogeneous “floating spheres” test cases originally
173 introduced during RAMI-1, 2) a “coniferous forest” scene
174 analogous to the Gaussian-hill canopy introduced during
175 RAMI-2 but without the topography, and 3) a “birch
176 stand” populated with trees of variable sizes and spec-
177 tral properties – intended primarily to enhance the de-
178 gree of structural realism amongst the RAMI test cases.
179 The new experiments complement those introduced dur-
180 ing earlier phases of RAMI, which focused primarily on
181 structurally homogeneous vegetation canopies (both in
182 the solar domain and under conservative scattering con-
183 ditions) but included also a small set of structurally het-
184 erogeneous plant canopies (see Section 2.1 in *Pinty et al.*
185 [2001] and Section 2 in *Pinty et al.* [2004b]). Exhaustive
186 documentation on the spectral and structural properties
187 of the various plant canopies (including the exact posi-
188 tion and orientation of individual leaves in the scenes with
189 discrete foliage representations, as well as the precise lo-
190 cation of all tree-like objects in the scene) were accessible
191 to the participants via the RAMI website. It was, how-
192 ever, left to the participants themselves to choose what
193 level of detail their model required in order to represent
194 at best the proposed canopy scenes.
195

196 Similar to previous phases of RAMI, participants were
197 encouraged to generate a standard set of 11 measure-
198 ments for every test case. These measurements in-
199 clude the total spectral Bidirectional Reflectance Factor
200 (BRF), in both the principal and the cross plane, together
201 with the corresponding contributions due to the single-
202 uncollided radiation scattered once by the soil only, the
203 single-collided radiation by the leaves or trees only, and
204 the radiation multiply collided by the leaves/trees/soil
205 system. Three flux quantities were also routinely asked
206 for, namely, the spectral albedo of the canopy (*i.e.*, the
207 directional hemispherical reflectance), the total transmis-
208 sion down to the underlying background, and, the total
209 absorption of radiation in the vegetation layer. In ad-
210 dition to these standard measurements, RAMI-3 intro-
211 duced two new measurement types, that applied, how-
212 ever, only to selected test cases. The first of these was a
213 local transmission transect measurement that was asked
214 for the “birch stand” experiment in order to assess the
215 ability of RT models to simulate *in-situ* measurement sit-
216 uations. Similarly, a horizontal flux measurement was
217 proposed for the “real-zoom-in” scene, that was first
218 introduced during RAMI-2 (section 2.2 in *Pinty et al.*
219 [2004b]), in order to document the performance of RT

220 models when estimating the magnitude of horizontal pho-
221 ton transport at various spatial resolutions in a struc-
222 turally heterogeneous canopy environment. Almost all
223 the RAMI measurements, whether directional or hemi-
224 spherical, had to be carried out with respect to a refer-
225 ence plane located at the top of canopy height level.

226
227 Overall a total of 464,816 (2,112) individual BRF
228 (flux) simulations were received at the JRC. In order
229 to pursue the analysis of these data beyond a mere vi-
230 sual comparison a protocol is needed that permits the
231 quantitative evaluation of RT model simulations despite
232 the lack of absolute reference standards (*i.e.*, in general
233 the true solution is not known). *Oreskes et al.* [1994],
234 and many others since, maintain that—under these lat-
235 ter conditions—the complete validation/verification of a
236 model is quite impossible, and that any such endeavour
237 should focus instead on showing the opposite, that is,
238 the onset of flaws in a model’s behaviour. RAMI thus
239 proposes a three-step procedure to identify incongruous
240 RT models: 1) by assessing the absence of inconsistencies
241 in the internal RT formulation of a model, 2) by verify-
242 ing the accurate and reliable performance of a model in
243 the limited number of cases where analytical solutions
244 are available, and 3) by comparing the output of a model
245 against a “surrogate truth” that is to be established from
246 credible candidates within the ensemble of available RT
247 simulations. Obviously the latter will only be meaning-
248 ful if sufficient consensus exists among the simulation re-
249 sults of RT models, in particular those that are known to
250 minimise the number of simplifications/approximations
251 in their radiative transfer formulation. The objective of
252 this three-step procedure thus lies in identifying RT mod-
253 els that deviate from the norm rather than boosting the
254 credibility of those models that do not differ. In fact,
255 conformity with the anticipated outcome in each one of
256 the above steps is not proof of a model’s physical cor-
257 rectness. Hence any claims regarding the credibility of a
258 model’s performance should be avoided, or—if they have
259 to be made—should always be limited to the set of pre-
260 scribed conditions under which the models were actually
261 tested.

262
263 In general, RT simulation models are rarely completely
264 amiss, nor, totally correct for that matter, but tend to lie
265 somewhere in between these two extremes. The quality of
266 their simulations is often subject to the degree by which
267 a given set of experimental conditions satisfies the struc-
268 tural, spectral and/or radiative premises on which the
269 models are based. In the context of RAMI, for example,
270 models often do not share the same internal representa-
271 tion or “image” of the prescribed canopy structure². Such
272 architectural deviations may often form the basis for sub-
273 sequent differences in simulation results – as will be seen
274 in sections 3 and 4. In addition to possible (structure and
275 illumination related) differences in the starting premises
276 of RT models, the precise manner in which certain RT
277 quantities are simulated may also vary, *e.g.*, the width of
278 the solid angle over which BRFs are computed may vary.
279 The identification of suitable limits describing the thresh-
280 old between valid and invalid models thus has to account
281 for these idiosyncrasies, and should preferably be formu-
282 lated in conjunction with criteria relating to the usage of
283 these models. For example, by incorporating the abso-
284 lute calibration accuracy of current space borne sensors
285 and/or the anticipated quality of state-of-the-art atmo-
286 spheric correction schemes into the evaluation scheme. In
287 the next section the above three-step invalidation proce-
288 dure will be applied to an ensemble of RAMI test cases for

289 which analytical solutions are available in a few isolated
290 cases, and so-called “surrogate truths” may be derived
291 for others, *e.g.*, *Pinty et al.* [2001, 2004b].

3. The RAMI baseline scenarios

292 All the forward-mode experiments that were proposed
293 during RAMI-1 have featured in subsequent phases of
294 the RAMI activity. These “baseline scenarios” can be
295 subdivided into two separate architectural classes: The
296 first one consists of structurally homogeneous canopies
297 that feature finite-sized (discrete) or point-like (turbid)
298 foliage elements that are randomly distributed within the
299 volume of a horizontally infinite vegetation layer bounded
300 by some top-of-canopy (TOC) level, as well as a lower
301 flat background surface. The second category relates
302 to structurally heterogeneous “floating spheres” environ-
303 ments where the (discrete or turbid) foliage elements are
304 randomly distributed within a series of spherical volumes
305 that are themselves freely floating above an underlying
306 flat background surface (for a graphical depiction see the
307 inlaid pictures in Figure 1). In both categories the direc-
308 tional scattering properties of the foliage and background
309 are Lambertian, and the orientation of the foliage ele-
310 ments follow predefined leaf normal distributions (LND),
311 *i.e.*, *Bunnik* [1978] and *Goel and Strelak* [1984]. By vary-
312 ing the illumination conditions, as well as the number,
313 size, orientation and spectral properties of the foliage
314 elements in the canopy (*idem* for the background bright-
315 ness) up to 52 structurally homogeneous and 8 “floating
316 spheres” baseline scenarios were defined. In the struc-
317 turally homogeneous case, a “purist corner” was included
318 where the spectral leaf and soil properties are such as to
319 test model performance in the limit of conservative scat-
320 tering conditions, *i.e.*, the soil brightness ($\alpha = 1$) and
321 the single-scattering albedo ($r_L + t_L = 1$) are unity, and
322 the leaf reflectance (r_L) is equal to the leaf transmittance
323 (t_L).

324
325 Figure 1 provides examples of the spread between
326 the various RT models that participated in the base-
327 line scenarios during RAMI-3. Shown are bidirectional
328 reflectance factor (BRF) simulations along the principal
329 (top panels) and orthogonal (bottom panel) planes
330 for structurally homogeneous (left panels) and heteroge-
331 neous “floating spheres” (right panels) canopies. The top
332 panels feature finite-sized disc-shaped foliage elements of
333 infinitesimal thickness (radius 0.1 m), whereas the bot-
334 tom panels relate to turbid medium canopies, *i.e.*, having
335 infinitesimally small but oriented scatterers. The spectral
336 properties of the canopy constituents in the top (bottom)
337 panels are typical for vegetation and bare soils in the red
338 (NIR) spectral domain. The illumination zenith angle
339 (θ_i) was set to 20° in all these cases. The panels of Fig-
340 ure 1 exemplify the degree and variability of agreement
341 between the various participating models. In particular,
342 in the case of the structurally homogeneous test cases
343 it is only the BRF simulations of the MBRF model in the
344 turbid medium case (lower left panel), and, to a lesser ex-
345 tent, the ACRM model in the discrete case (top left panel)
346 that are different. The deviations of the MBRF model
347 in the NIR may be largely explained by its usage of a
348 “two-stream” approximation when estimating the multiple
349 collided BRF component. At the same time the agree-
350 ment between the FLIGHT, drat, Rayspread, raytran,
351 and Sprint3 Monte Carlo models is striking for both the
352 homogeneous and heterogeneous test cases. Somewhat
353 different from these 5 models—and each other—are the
354 simulation results for DART, MAC, FRT, 4SAIL2, and 5Scale

355 in the turbid and/or discrete “floating spheres” test cases.

356
357 Despite the visually noticeable dispersion of some of
358 the model contributions in Figure 1, one should—in
359 general—refrain from speculative guesses about potential
360 outliers without a careful examination of the exact con-
361 ditions under which the various models were executed.
362 One of the first aspects to verify is the faithful repre-
363 sentation of the prescribed architectural canopy char-
364 acteristics. It is now well accepted that multi-angular
365 observations are sensitive to the structure of a given
366 canopy target, *e.g.*, *Gerard and North* [1997]; *Widlowski*
367 *et al.* [2001]; *Lovell and Graetz* [2002]; *Chopping et al.*
368 [2003]; *Chen et al.* [2003]; *Rautiainen et al.* [2003]. By
369 the same token, deviations from the structural charac-
370 teristics of a given RAMI scene may thus translate itself
371 into the model-simulated magnitude (and shape) of the
372 TOC BRF field. During RAMI-3 almost all of the par-
373 ticipating models differed in their structural premises—
374 either systematically or occasionally—from those pre-
375 scribed on the RAMI website. For example, the **ACRM**
376 and **MBRF** models both use elliptical equations [*Campbell*,
377 1990] rather than beta-functions or geometric formula-
378 tions to describe the LNDs of the foliage elements; **DART**
379 approximates the “floating spheres” by a series of small
380 cubes; **Hyemalis** reduced the physical dimensions of the
381 proposed scenes to deal with internal computer memory
382 requirements; **MAC**, **FRT** and **5Scale** assume a statistical—
383 that is, random—spatial distribution of the objects in a
384 scene rather than implementing the spatially explicit lo-
385 cations prescribed on the RAMI website; **MBRF** uses rect-
386 angular leaves rather than disc-shaped ones; **RGM** emulates
387 leaf shapes by aggregating small triangular primitives;
388 and the **Sprint3** model always uses statistical distribu-
389 tions (rather than deterministic placements) of the foliage
390 elements. These structural deviations—which are often
391 motivated by the need for elegant and speedy solutions
392 to the RT equation—may, however, become relevant in
393 an intercomparison exercise like RAMI.

394
395 *Widlowski et al.* [2005] recently showed that vegeta-
396 tion canopies with identical domain-averaged state vari-
397 able values but different structural representations will,
398 in general, yield different multi-angular BRF patterns.
399 In the context of RAMI, one may thus expect differ-
400 ences to occur between RT models featuring exact rep-
401 resentations of the prescribed canopy structures and 1)
402 improved/expanded versions of essentially plane-parallel
403 RT models in simulations over structurally heterogeneous
404 canopy targets, or, 2) RT models that rely implicitly
405 on 3-D plant structures (*i.e.*, Geometric Optical models)
406 when applied to structurally homogeneous test cases. For
407 these reasons the **MAC (4SAIL2)** model, which utilises a pa-
408 rameterised formalism to distribute vegetation elements
409 (gaps) within each elevation of its (one or two layer) veg-
410 etation canopy representation, may deviate from the RT
411 quantities simulated using models that make use of the
412 actual location of vegetation elements in the heteroge-
413 neous RAMI test cases. Similarly, the simulations of the
414 **5Scale** model in the context of 1-D canopies have not
415 been included in this manuscript.

416
417 In order to obtain a comprehensive indication of the
418 performance of a RT model in forward mode, it is essen-
419 tial to run it on as large an ensemble of structurally and
420 spectrally different canopy scenarios as possible – with-
421 out, however, compromising the structural premises on
422 which its internal canopy representation is based. Thus,
423 the greater the degree of realism and the larger the struc-

424 tural diversity of the available number of RAMI test cases
 425 is, the more indicative the observed BRF deviations be-
 426 tween the various RT models and/or some “surrogate
 427 truth” will become. Last but not least, one should also
 428 note that the performance of many 1-D and 3-D RT mod-
 429 els could always be improved through the usage of more
 430 precise numerical integration schemes, as well as, larger
 431 numbers of ray trajectories in the case of some of the MC
 432 models. Such a “tuning” of model performances would,
 433 however, be of little interest to model users if 1) the pub-
 434 lically available versions of these computer codes cannot
 435 deliver these accuracies, and 2) the computation times to
 436 achieve such accuracies become prohibitive in the daily
 437 usage of the models.

438
 439 When constrained to evaluate model simulations in the
 440 absence of any absolute reference standard or “truth”, as
 441 is the case with RAMI, *Pinty et al.* [2001] argued that
 442 RT model benchmarking on the basis of statistical mo-
 443 ments, derived from the entirety of participating models,
 444 may be biased in the presence of outliers. Instead they
 445 proposed a relative evaluation scheme where the simu-
 446 lations of individual models are compared against those
 447 from all other participating models over as large as pos-
 448 sible a set of conditions. In this way, RT models that
 449 are consistently different from others can be identified
 450 [*Pinty et al.*, 2004b]. The same authors also note that
 451 internal inconsistencies in one or more submodules of a
 452 given RT model may compensate each other and lead
 453 to apparently correct overall BRF estimates. They thus
 454 recommend the evaluation of BRF components as well as
 455 the total BRFs generated by a model. In the following,
 456 the three-step invalidation procedure from section 2 will
 457 be applied to both the homogeneous and heterogeneous
 458 baseline scenarios of RAMI-3. More specifically, subsec-
 459 tion 3.1 will investigate the internal self-consistency of
 460 the models that participated in the baseline scenarios of
 461 RAMI-3. Subsection 3.2 then looks at RT model per-
 462 formance in situations where exact analytical solutions
 463 are available. Finally, subsection 3.3 documents various
 464 aspects of relative model intercomparison with respect
 465 to the discrete homogeneous and the “floating spheres”
 466 baseline scenarios.

3.1. Model self-consistency

467 It is difficult to offer meaningful interpretations as to
 468 why the output of a given RT model may be different
 469 from simulation results of other models without verifi-
 470 cation of the models’ internal consistency. Energy con-
 471 servation, for example, is one of the key principles to
 472 ensure, and this both with respect to directional (BRFs)
 473 and hemispherically integrated (fluxes) quantities.

3.1.1. Energy conservation

476 The solar radiation entering a plant canopy is parti-
 477 tioned into an absorbed A , a reflected R and a trans-
 478 mitted T fraction such that all incident photons are
 479 accounted for. Energy conservation thus requires that
 480 $A + R + (1 - \alpha)T = 1$, where α is the soil brightness. The
 481 capacity of a given model (m) to conserve energy can be
 482 described using:

$$\Delta_{\text{F}}(m) = \frac{1}{N_{\text{F}}(m)} \sum_{\lambda=1}^{N_{\lambda}^m} \sum_{\zeta=1}^{N_{\zeta}^m} \sum_{i=1}^{N_{\Omega_i}^m} \left[A_m(\lambda, \zeta, i) + R_m(\lambda, \zeta, i) \right]$$

$$+[1 - \alpha(\lambda)] T_m(\lambda, \zeta, i) \Big] - 1$$

483 where $N_F(m) = N_\lambda^m + N_\zeta^m + N_{\Omega_i}^m$ is the total number
 484 of spectral λ , structural ζ , and illumination Ω_i condi-
 485 tions for which flux simulations were performed by model
 486 m . Figure 2 shows the mean deviation from energy con-
 487 servation, $\Delta_F(m)$ for those models that simulated flux
 488 quantities in the case of the structurally homogeneous
 489 baseline scenarios. More specifically, the top panel dis-
 490 plays $\Delta_F(m)$ for canopies with discrete leaves in the solar
 491 domain, and the bottom panel shows $\Delta_F(m)$ for turbid
 492 medium canopies with conservative scattering properties
 493 (purist corner). It should be noted that the **MAC** model
 494 seems to generate an excess of energy ($\Delta_F(\text{MAC}) > 0$)
 495 that is equivalent to about 3% of the incident radiation
 496 at the TOC in the solar domain. On the other hand,
 497 the **FLIGHT** and **raytran** models both appear to lose en-
 498 ergy ($\Delta_F < 0$), equivalent to $\sim 2\%$ of the incident radi-
 499 ation at those wavelengths. Under conservative scattering
 500 conditions, however, the latter two models comply very
 501 well with energy conservation requirements ($\Delta_F \approx 0$),
 502 a pattern that is observed for both discrete and tur-
 503 bid medium foliage representations in structurally ho-
 504 mogeneous, as well as heterogeneous environments (not
 505 shown). Since $\alpha = 1$ under purist corner conditions it
 506 must be the canopy transmission measurement that af-
 507 fects Δ_F for both **FLIGHT** and **raytran**. Indeed, in the
 508 case of **raytran** it turned out that the diffuse transmis-
 509 sion component had been neglected in the submitted
 510 simulations. By the same token the deviations of the
 511 **DART** model under conservative scattering conditions are
 512 likely to arise from its estimation of the canopy absorp-
 513 tion and/or reflectance. Further analysis (not shown)
 514 indicated that enhanced multiple scattering conditions
 515 exacerbate the apparent deviations from energy conser-
 516 vation for all models with non-zero Δ_F values in Figure 2.
 517 As to how much these apparent deviations from energy
 518 conservation relate to model deficiencies rather than op-
 519 erator errors is, however, difficult to anticipate. By the
 520 same token, RT models that utilise the principle of en-
 521 ergy conservation to close their radiation budget will ob-
 522 viously never be found deviating in such self-consistency
 523 checks. This applies, for example, to the **1/2-discret**,
 524 **Sail++** and **2-Stream** models which derive their canopy
 525 absorption estimate from simulations of the reflectance
 526 and transmission properties of the vegetation layer.
 527

528 3.1.2. BRF consistency

529 The RAMI format specifications ask for all radiative
 530 quantities to be provided with a precision of six decimal
 531 places, *i.e.*, the implicit error associated with the mea-
 532 surements is thus of the order of 10^{-6} . The average ab-
 533 solute difference $\Delta\rho$ between the total BRF (ρ_{tot}) and the
 534 sum of the BRF contributions due to the single uncollided
 535 (ρ_{uc}), the single-collided (ρ_{co}), and the multiple-collided
 536 (ρ_{mt}) radiation components should thus be of a similar
 537 magnitude when defined as follows:

$$\begin{aligned}
 \Delta\rho(m) = & \frac{1}{N_\rho(m)} \sum_{\lambda=1}^{N_\lambda^m} \sum_{\zeta=1}^{N_\zeta^m} \sum_{v=1}^{N_{\Omega_v}^m} \sum_{i=1}^{N_{\Omega_i}^m} \left| \rho_{tot}^m(\lambda, \zeta, v, i) \right. \\
 & \left. - [\rho_{uc}^m(\lambda, \zeta, v, i) + \rho_{co}^m(\lambda, \zeta, v, i) + \rho_{mt}^m(\lambda, \zeta, v, i)] \right|
 \end{aligned}$$

538 where $N_\rho(m) = N_\lambda^m + N_\zeta^m + N_{\Omega_v}^m + N_{\Omega_i}^m$ is the total
 539 number of BRFs that were generated with the model m

540 for different spectral λ , structural ζ , viewing Ω_v , and
 541 illumination Ω_i conditions. Apart from **Hyemalis** and
 542 **2-Stream**, all models in Table 1 provided simulations of
 543 the three BRF components for at least some of the test
 544 cases of RAMI-3. In general, the average absolute deviation
 545 $\Delta\rho$ was $< 10^{-5}$, with the exception of $\Delta\rho(\mathbf{5Scale}) =$
 546 0.0027 for the discrete homogeneous solar domain, as well
 547 as $\Delta\rho(\mathbf{frat}) = 0.0013$ and $\Delta\rho(\mathbf{FLIGHT}) = 0.0002$ for the
 548 homogeneous discrete purist corner. These deviations,
 549 although small in terms of the magnitude of the total
 550 BRF and often related to the configuration of the model
 551 in its day to day usage, are nevertheless significant in the
 552 context of a model intercomparison exercise like RAMI
 553 since—by their statistical nature—they seem to indicate
 554 that some of the models do not conserve energy when
 555 partitioning the total BRF into its various subcomponents.
 556

557 3.1.3. Spectral ratio of the single-uncollided BRF

559 Model self-consistency can also be evaluated across
 560 different wavelengths. The ratio $\rho_{uc}(\lambda_1)/\rho_{uc}(\lambda_2)$ of the
 561 single-uncollided BRF components in the red and NIR
 562 spectral regimes, for example, relates to the differing
 563 amounts of radiation that have been scattered once by
 564 the underlying background (and never interacted with
 565 the canopy foliage) at these two wavelengths (λ_1 and λ_2).
 566 In the case of Lambertian soils, this spectral ratio must
 567 be a directionally invariant constant equal to the ratio
 568 of the soil albedos at the wavelengths of interest, *i.e.*,
 569 $\alpha(\lambda_1)/\alpha(\lambda_2)$. Ensemble-averaging over a variety of structure
 570 ζ and illumination Ω_i conditions ($N_S = N_\zeta^m + N_{\Omega_i}^m$)
 571 then provides an indication of the average deviation from
 572 spectral consistency for any model m :

$$\Delta_S(m, \Omega_v) = \frac{\alpha(\lambda_1)}{\alpha(\lambda_2)} - \left[\frac{1}{N_S(m)} \sum_{\zeta=1}^{N_\zeta^m} \sum_{i=1}^{N_{\Omega_i}^m} \frac{\rho_{uc}^m(\lambda_1, \zeta, \Omega_v, i)}{\rho_{uc}^m(\lambda_2, \zeta, \Omega_v, i)} \right]$$

573 Figure 3 documents the angular variation of Δ_S , obtained
 574 from single-uncollided BRF simulations in the red and
 575 NIR spectral domains, for homogeneous turbid medium
 576 (left) and discrete floating-spheres canopies (right) hav-
 577 ing uniform LNDs. Not included in these graphs are
 578 the forward MC ray-tracing models **frat** and **raytran**
 579 due to the large noise levels associated with their sam-
 580 pling schemes. MC noise is also evident for the **drat** and
 581 **Rayspread** models, although this decreases as more rays
 582 are being used in the RT simulation and/or the fraction
 583 of the contributing background in the scene increases,
 584 *e.g.*, in the “floating spheres” scenarios. One will notice
 585 that, with the exception of the **Sprint3** model in the
 586 “floating spheres” case, the spectral ratio of the single-
 587 uncollided BRF component remains relatively constant
 588 for all models (including **ACRM** in the homogeneous dis-
 589 crete case – not shown) up to view zenith angles of about
 590 $65 - 70^\circ$. The **Sprint3** model, and to a lesser extent
 591 also the **Rayspread** model, utilise a variance reduction
 592 technique known as “photon spreading” in order to re-
 593 duce the number of rays that sample the radiative trans-
 594 fer properties of the medium of interest. In Figure 3
 595 the deviations in the magnitude but not in the shape
 596 of the single-uncollided BRF components in the homo-
 597 geneous turbid case (left panel) may thus be solely due
 598 to an insufficient sampling (LAI=3) of the lower bound-
 599 ary condition contributing to ρ_{uc} . On the other hand,
 600 the variations of $\Delta_S(\mathbf{Sprint3})$ with view zenith angle in
 601 the “floating spheres” case (LAI=2.36) may be due to

602 the spatially varying presence of foliage in the canopy to-
 603 gether with the statistical distribution of foliage—rather
 604 than a deterministic placement of scatterers—within the
 605 various spherical volumes. As such the actual number
 606 of rays, that traverse the floating spheres (LAI=5) and
 607 reach the ground or escape the scene unhindered, is never
 608 the same in different directions if model runs at different
 609 wavelengths do not use the same starting seeds to ini-
 610 tialise their random number generator.

3.2. Absolute model performance

611 Exact analytical solutions to the radiative transfer
 612 equation do not exist for the vast majority of conceiv-
 613 able vegetation canopies. In some cases, however, the
 614 structural and spectral properties of vegetated surfaces
 615 may be such that it becomes possible to predict at least
 616 some of their radiative properties analytically. Within
 617 the available set of RAMI test cases there are at least two
 618 different types of absolute model evaluations that can be
 619 performed: The first one relates to single-collided BRF
 620 components of structurally homogeneous turbid medium
 621 canopies with uniform LND, and the second to the re-
 622 flected and absorbed energy fluxes in the various conser-
 623 vative scattering (purist corner) scenarios.

624

3.2.1. Homogeneous turbid uniform canopy

625 Structurally homogeneous leaf canopies with az-
 626 imuthally invariant uniform LNDs are characterised by
 627 a constant probability of foliage interception irrespective
 628 of the direction of propagation in that medium [Ross,
 629 1981; Verstraete, 1987]. In addition, turbid media—with
 630 their infinitesimally small scatterers—satisfy the far field
 631 approximation and thus never yield a hot spot, *i.e.*, a
 632 localised increase in the BRF around the retro-reflection
 633 direction of the incident illumination, *e.g.*, Gerstl [1988];
 634 Verstraete [1988]; Kuusk [1991]. The single-uncollided
 635 BRF component of such a canopy can be written as:
 636

$$\rho_{uc}(\Omega_i, \Omega_v) = \alpha \exp \left[\frac{-\text{LAI}(\mu_i + \mu_v)}{2\mu_i\mu_v} \right]$$

637 where α is the albedo of the Lambertian soil, $\mu = \cos \theta$
 638 is the cosine of the illumination (i) or view (v) zenith
 639 angle $0 \leq \theta \leq \pi/2$, and LAI is the leaf area index of the
 640 canopy. Similarly the single-collided BRF component of
 641 such a canopy can be written as:

$$\rho_{co}(\Omega_i, \Omega_v) = \frac{2\Gamma(\Omega_i \rightarrow \Omega_v) \left[1 - \exp \frac{-\text{LAI}(\mu_i + \mu_v)}{2\mu_i\mu_v} \right]}{\mu_i + \mu_v}$$

642 where the canopy scattering phase function is given by
 643 [Shultis and Myneni, 1988]:

$$\Gamma(\Omega_i \rightarrow \Omega_v) = \frac{r_L + t_L}{3\pi} (\sin \beta - \beta \cos \beta) + \frac{t_L}{3} \cos \beta$$

644 and β is the phase angle between the illumination and
 645 viewing direction:

$$\cos \beta = \cos \theta_i \cos \theta_v + \sin \theta_i \sin \theta_v \cos |\phi_i - \phi_v|$$

646 and r_L (t_L) is the reflectance (transmittance) of the fo-
 647 liage elements. Figure 4 shows the mean absolute error
 648 between RT model simulations and the above analyti-
 649 cal formulations for the single-collided (left panel) and
 650 the single-uncollided (right panel) BRF components of

651 a turbid medium canopy with uniform LND and Lam-
652 bertian scattering laws. The averaging was performed
653 over BRF simulations in the principal and orthogonal
654 planes, as well as, for illumination zenith angles of 20°
655 and 50° . With the exception of **MBRF** all RT models lie
656 within 0.0025 of the truth in the single-collided case. The
657 operator of the **MBRF** model conjectures, however, that
658 the observed deviations may be due to a software error
659 (bug) since the formulation of the single-collided BRF
660 component in *Qin and Xiang* [1997] is based on a proper
661 theoretical derivation. In the single-uncollided case the
662 agreement between the participating RT models and the
663 analytical solution is ten times better still than in the
664 single-collided case, *i.e.*, all models lie within $2.5 \cdot 10^{-4}$
665 of the analytical solutions. This is impressive since the
666 magnitude of ρ_{co} (ρ_{uc}) along the orthogonal plane was
667 typically around 0.017 (0.003) in the red and 0.16 (0.005)
668 in the NIR. Furthermore, it should be noted that none of
669 the participants had any *a priori* knowledge about these
670 absolute evaluation tests. In principle, the performance
671 of many of the participating RT models could thus still be
672 improved further, for example, by increasing the number
673 of integration steps (*e.g.*, Gaussian quadrature points)
674 in numerical techniques, or, by adding further rays to
675 sample the characteristics of the canopy-leaving radia-
676 tion field (in the case of MC ray-tracing models).

677

678 3.2.2. Purist corner fluxes

679 Under conservative scattering conditions all of the en-
680 ergy that enters a canopy system has to leave it, *i.e.*,
681 $R = 1$ and $A = 0$. The RAMI purist corner thus pro-
682 vides another opportunity to assess the performance of
683 RT models against a known absolute reference. Figure 5
684 shows (on a log-log scale) the average absolute deviation ε
685 from the true canopy absorption (y-axis) and reflectance
686 (x-axis) for homogeneous canopies with finite-sized (left
687 panel), as well as turbid medium (right panel) foliage rep-
688 resentations under conservative scattering properties. In
689 each case the averaging was performed over ($N = 18$) test
690 cases with different LAI, LND and θ_i . With the excep-
691 tion of **MBRF**, which did not provide absorption estimates,
692 all models featuring $\varepsilon = 10^{-7}$ (or -7 in Figure 5) sub-
693 mitted the theoretical values. In the homogeneous turbid
694 case, for example, both the **raytran**, and **Sprint3** models
695 compute the canopy absorption and reflectance to within
696 computer-precision uncertainties. The **1/2-discret** and
697 **2-Stream** models, on the other hand, showed an aver-
698 age absolute deviation of 0.0015 and 0.0245, respectively,
699 for both $\varepsilon_{\text{Absorption}}$ and $\varepsilon_{\text{Reflectance}}$. Models that fall on
700 the 1:1 line in Figure 5 estimate their canopy absorp-
701 tion by closing the energy budget. In the case of the
702 **1/2-discret** model the (negative) canopy absorption de-
703 viations arose from overestimated albedos under the fully
704 scattering purist corner conditions. These in turn, are a
705 consequence of the fixed number (16) of Gaussian quadra-
706 ture points used in the numerical integration scheme of
707 the azimuthally averaged multiple-scattering component.
708 The **DART** model, on the other hand, which computes
709 canopy absorption on a ray-by-ray basis, features a re-
710 spectable $\varepsilon_{\text{Absorption}} = 0.0006$ and $\varepsilon_{\text{Reflectance}} = 0.0125$.
711 In the discrete homogeneous case (right panel), the av-
712 erage absolute deviation of the **1/2-discret** model from
713 the correct absorption and reflectance values increases to
714 0.0204, presumably due to highly variable BRFs in the
715 vicinity of the retro-reflection direction (hot spot) that af-
716 fected the accuracy of the numerical integration scheme.
717 At this point, one should recall that the lack of deviations
718 from the “truth” is not a proof of the physical correctness

719 of a model since, for example, hard-encoded program-
 720 ming statements may be contained inside the computer
 721 code that do account for the eventuality of situations for
 722 which the exact solution is known. In this way, the ac-
 723 tual model would not be executed—to compute canopy
 724 reflectance and absorption here—but sidestepped to gener-
 725 ate the anticipated results. The primary interest here
 726 (and in all other parts of section 3) thus lies in under-
 727 standing the observed *deviations* from the correct solu-
 728 tion.

3.3. Relative model performance

729 Without access to absolute reference standards the
 730 evaluation of RT models has to rely on relative model
 731 intercomparison. The goal being to identify systematic
 732 trends in the behaviour of one (or more) models with
 733 respect to others, over ensembles of test cases. Three
 734 different types of relative intercomparison metrics will
 735 be proposed here: model-to-model deviations, model-to-
 736 ensemble deviations, and deviations from model-derived
 737 surrogate truths.

3.3.1. Model-to-model deviations

740 The differences in the BRF simulations between two
 741 models (c and m), when averaged over a variety of spec-
 742 tral (λ), structural (ζ), viewing (Ω_v) and illumination
 743 (Ω_i) conditions, can be defined as:

$$\delta_{m \leftrightarrow c} = \frac{200}{N} \sum_{\lambda=1}^{N_\lambda} \sum_{\zeta=1}^{N_\zeta} \sum_{v=1}^{N_{\Omega_v}} \sum_{i=1}^{N_{\Omega_i}} \left| \frac{\rho_m(\lambda, \zeta, v, i) - \rho_c(\lambda, \zeta, v, i)}{\rho_m(\lambda, \zeta, v, i) + \rho_c(\lambda, \zeta, v, i)} \right|$$

744 where $N = N_\lambda + N_\zeta + N_{\Omega_v} + N_{\Omega_i}$ is the total number
 745 of BRF simulations that have been performed by both
 746 models c and m , and $\delta_{m \leftrightarrow c}$ is expressed in percent.

747 Figure 6 depicts a series of two-dimensional grids con-
 748 taining information on the various model-to-model BRF
 749 differences (blue-red colour scheme in the lower right half
 750 of each panel), as well as, the percentage of the total
 751 number of BRFs over which the $\delta_{m \leftrightarrow c}$ values were de-
 752 rived (black-green colour scheme in upper left half of each
 753 panel). More specifically, $\delta_{m \leftrightarrow c}$ is shown for those models
 754 having submitted the total (top row), single-uncollided
 755 (second row), single-collided (third row) and multiple-
 756 collided (bottom row) BRF data for structurally homo-
 757 geneous canopies with finite-sized (leftmost column) and
 758 turbid medium (middle-left column) foliage representa-
 759 tions, as well as, for “floating spheres” scenarios with
 760 finite-sized (middle-right column) and turbid medium
 761 (rightmost column) foliage representations in the solar
 762 domain. The blue colour scale increments in steps of
 763 2%, the green colour scale in steps of 10%, and the red
 764 also in steps of 10% with the bright red colour indicat-
 765 ing values larger than 50%. The maximum number of
 766 BRF simulations included in the computation of $\delta_{m \leftrightarrow c}$
 767 was 1216 for the structurally homogeneous and 608 for
 768 the “floating spheres” canopies. To illustrate the reading
 769 of the various panels in Figure 6 let’s consider, for exam-
 770 ple, the total BRFs of the **Hyemalis** and **Sprint3** models
 771 in the discrete homogeneous case (top left panel): Their
 772 model-to-model difference value, which lies between 10
 773 and 20% (light red colour), has been obtained from less
 774 than 10% of the total number of BRF simulations (dark
 775 green colour) and thus may not be too representative.
 776 On the other hand, the $\delta_{m \leftrightarrow c}$ of the **ACRM** and **Sprint3**
 777 models (same top left panel) lies somewhere between 6
 778 and 8% and has been established using 100% of the pos-

779 sible BRFs. In general, the majority of models in the
780 discrete and turbid homogeneous cases agree rather well
781 with each other ($\delta_{m \leftrightarrow c} < 10\%$). This behaviour is also
782 present for the various BRF components with the ex-
783 ception of the single-uncollided BRF component (ρ_{uc}) in
784 the discrete homogeneous case where the various imple-
785 mentations/approximations of the hot spot phenomenon
786 have increased the differences amid the simulated BRFs.
787 In the case of turbid homogeneous canopies the DART
788 model features somewhat elevated $\delta_{m \leftrightarrow c}$ values for the
789 ρ_{uc} component which may, however, be partly due to
790 the inter/extrapolation procedure that had to be sys-
791 tematically applied to all BRF simulations of this model
792 in order to map its submitted 32 (18) viewing condi-
793 tions in the principal (orthogonal) plane to the full set
794 of 76 as specified by RAMI. The FLIGHT model—which
795 did not update its baseline scenario simulations during
796 RAMI-3—shows slightly diverging multiple-collided BRF
797 components in both the discrete and turbid medium ho-
798 mogeneous cases. These are caused by a Lambertian
799 assumption governing the angular distribution of higher
800 orders of scattered radiation in simulation results origi-
801 nally submitted during RAMI-1. This effect is no longer
802 visible in the “floating spheres” case due to subsequent
803 model improvements in phase 2 (right panels in Fig-
804 ure 6). Unlike in the discrete homogeneous cases, the
805 “floating spheres” ρ_{uc} shows the smallest $\delta_{m \leftrightarrow c}$ values
806 presumably because the hotspot here is dominated by
807 the geometry of the spheres themselves. In the “float-
808 ing spheres” cases it is thus the multiple scattering and
809 to a lesser extent also the single-collided BRF compo-
810 nents that show the largest differences between BRF sim-
811 ulations of 3-D Monte Carlo models—featuring explicit
812 scene representations—and those of somewhat more ap-
813 proximate models.

814

815 3.3.2. Model-to-ensemble deviations

816 In the absence of any absolute reference truth, the out-
817 put from individual RT models may also be compared
818 to ensemble averages computed from simulation results
819 of other RT models, as first proposed by *Pinty et al.*
820 [2001, 2004b]. In this way, RT models that are very differ-
821 ent from all other models can be identified and—although
822 not wrong in any absolute sense—they may then be ex-
823 cluded from further iterations of the ensemble averaging
824 process, if this is deemed appropriate. For any spectral
825 (λ), structural (ζ), viewing (v), and illumination (i) con-
826 dition one can compute:

$$\delta_m(\lambda, \zeta, v, i) = \frac{200}{N_c} \sum_{c=1; c \neq m}^{N_c} \left| \frac{\rho_m(\lambda, \zeta, v, i) - \rho_c(\lambda, \zeta, v, i)}{\rho_m(\lambda, \zeta, v, i) + \rho_c(\lambda, \zeta, v, i)} \right|$$

827 where N_c is the number of models with which the output
828 of model m is to be compared. One way to analyse such
829 δ_m statistics is to bin them over a variety of conditions
830 in order to yield a histogram of model-to-ensemble de-
831 viations. The inlaid graphs in Figure 7 show a variety
832 of δ_m histograms generated from total BRF simulations
833 of the 1/2-discret, drat, FLIGHT, frat, Rayspread,
834 raytran, RGM, Sail++, Sprint3, and 4SAIL2 models in the
835 case of the discrete structurally homogeneous canopies
836 (left panel), and the drat, FLIGHT, Rayspread, raytran,
837 and Sprint3 models in the case of the discrete “float-
838 ing spheres” canopies (right panel). The main graphs
839 of Figure 7 show the outer envelope of these δ_m his-
840 tograms both for the discrete structurally homogeneous
841 canopies (left panel) and the discrete “floating spheres”

842 canopies (right panel). One will notice that the agree-
 843 ment between the RT models in RAMI-3 (red line) is
 844 better than the corresponding agreement of models dur-
 845 ing the previous phase of RAMI three years ago (black
 846 line). In the homogeneous baseline scenarios, where more
 847 models are included than during RAMI-2, the first peak
 848 of the histogram envelope ($0 \leq \delta_m \leq 2.5\%$) can be
 849 attributed primarily to the models **1/2-discret**, **drat**,
 850 **FLIGHT**, **Rayspread** and **raytran**. The second half of the
 851 histogram envelope ($\delta_m > 2.5\%$), on the other hand,
 852 arises from BRF simulations due to the models **frat**,
 853 **MAC**, **RGM**. The models **Sail++** and **Sprint3**—with their
 854 broader distributions of δ_m —contribute to both parts of
 855 the histogram envelope.

856
 857 Alternatively one may define an overall indicator of
 858 model-to-ensemble differences, $\bar{\delta}_m$ [%] by averaging the
 859 above $\delta_m(\lambda, \zeta, v, i)$ over appropriate sets (\bar{N}) of spectral
 860 λ , structural ζ , viewing v and illumination i conditions:

$$\bar{\delta}_m = \frac{1}{\bar{N}} \sum_{\lambda=1}^{N_\lambda} \sum_{\zeta=1}^{N_\zeta} \sum_{v=1}^{N_{\Omega_v}} \sum_{i=1}^{N_{\Omega_i}} \delta_m(\lambda, \zeta, v, i)$$

861 Table 2 shows the values of the overall model disper-
 862 sion indicator $\bar{\delta}_m$ [%] obtained from an ensemble of six
 863 3-D Monte Carlo models, namely: **DART**, **drat**, **FLIGHT**,
 864 **Rayspread**, **raytran** and **Sprint3**. For each one of these
 865 models $\bar{\delta}_m$ is provided for the total BRF (ρ_{tot}) as well as
 866 the single-collided (ρ_{co}), the multiple-collided (ρ_{mt}), and
 867 the single-uncollided (ρ_{uc}) BRF components using sub-
 868 mitted simulation results from either RAMI-2 or RAMI-
 869 3. With the exception of the total BRF simulations of
 870 **DART** all other $\bar{\delta}_m$ values improved between RAMI-2 and
 871 RAMI-3, meaning that a smaller dispersion exists be-
 872 tween the BRF values of the latest version of these mod-
 873 els. The average dispersion between the total BRF sim-
 874 ulations of the six 3-D MC models was found to have
 875 almost halved from RAMI-2 (1.37 %) to RAMI-3 (0.72
 876 %) in the discrete case, and in the turbid medium case
 877 it improved by a factor of ~ 7 from RAMI-2 (6.36 %) to
 878 RAMI-3 (0.91 %).

879 3.3.3. Model-to-surrogate-truth deviations

881 Monte Carlo RT models allow for explicit 3-D repre-
 882 sentations of complex canopy architectures by describing
 883 these environments with (sometimes Boolean combina-
 884 tions of) sufficiently small geometric building blocks of
 885 known radiative properties. Solving the radiative trans-
 886 fer equation for such 3-D environments is then achieved
 887 through a stochastic sampling of the surface-leaving ra-
 888 diation field [Disney et al., 2000]. Since this is a time
 889 consuming undertaking—in particular for complex 3-D
 890 scenes—the current generation of 3-D MC models dif-
 891 fer primarily in the amount of deterministic detail that is
 892 used when constructing a scene, and, in the approach and
 893 extent to which ray trajectories are sampled within the
 894 3-D media. Both Figure 6 and Table 2 indicate that the
 895 3-D Monte Carlo models, **DART**, **drat**, **FLIGHT**, **Rayspread**,
 896 **raytran** and **Sprint3** are generally in very close agree-
 897 ment with each other. In particular the numbers in Ta-
 898 ble 2 support their usage in attempts to provide a “sur-
 899rogate truth” estimate against which further RT model
 900 comparisons may then be carried out. One simple way to
 901 obtain a “surrogate truth” estimate is by averaging the
 902 BRFs obtained from a set of $N_{3D}^{credible}$ credible 3-D MC
 903 models, that is:

$$\bar{\rho}_{3D}(\lambda, \zeta, v, i) = \frac{1}{N_{3D}^{credible}} \sum_{n=1}^{N_{3D}^{credible}} \rho_{3D}(\lambda, \zeta, v, i; n)$$

904 where the precise number and names of the 3-D MC mod-
 905 els that feature within $N_{3D}^{credible}$ is selected from among
 906 the following models: **DART**, **drat**, **FLIGHT**, **Rayspread**,
 907 **raytran** and **Sprint3**. The selection procedure is ap-
 908 plied to every RAMI experiment and measurement type
 909 individually and adheres to the following list of criteria:

- 910 • For every RAMI BRF (flux) measurement, identify
 911 at least two (one) 3-D Monte Carlo models that do not
 912 belong to the same RT modelling school/family,
 913
- 914 • If two models from the same RT modelling
 915 school/family are available, *e.g.*, **Rayspread** and **raytran**,
 916 choose the one with the least amount of apparent MC
 917 noise,
- 918 • Remove all those 3-D Monte Carlo models from the
 919 reference set that are noticeably different from the main
 920 cluster of 3-D MC simulations,
- 921 • If sufficient models are contained in the main cluster
 922 of 3-D MC simulations then remove those models that
 923 would introduce noticeable levels of “MC noise” into the
 924 reference set,
- 925 • If there are two distinct clusters of 3-D Monte Carlo
 926 models, or, no obvious cluster at all, then use all avail-
 927 able 3-D RT models to define a reference solution.

928
 929 A synoptic table featuring the names of the various
 930 3-D MC models that contribute toward the computa-
 931 tion of $\bar{\rho}_{3D}$ for all the RAMI-3 experiments and mea-
 932 surement types individually, can be found on the fol-
 933 lowing internet page: http://romc.jrc.it/WWW/PAGES/ROMC_Home/RAMIREF.html³.

934
 935
 936 Once the “surrogate truth” is available for the various
 937 RAMI baseline scenarios, the deviations of individual RT
 938 models from this norm may be quantified with the fol-
 939 lowing metric [Pinty *et al.*, 2004b]:

$$\chi_m^2(\lambda) = \frac{1}{N-1} \sum_{\zeta=1}^{N_\zeta} \sum_{v=1}^{N_{\theta_v}} \sum_{i=1}^{N_{\theta_i}} \frac{[\rho_m(\lambda, \zeta, v, i) - \bar{\rho}_{3D}(\lambda, \zeta, v, i)]^2}{\sigma^2(\lambda, \zeta, v, i)}$$

940 where $\sigma(\lambda, \zeta, v, i) = f \cdot \bar{\rho}_{3D}(\lambda, \zeta, v, i)$ corresponds to a
 941 fraction f of the average BRF obtained from the credible
 942 3-D Monte Carlo models.

943 Figure 8 displays the χ^2 values in the red and NIR
 944 wavelengths for the structurally homogeneous (left panel)
 945 and the “floating spheres” (right panel) baseline scenarios
 946 having finite-sized scatterers. Arrows indicate changes
 947 in the χ^2 values when comparing the performance of a
 948 model in RAMI-2 (base of arrow) with that in RAMI-
 949 3 (tip of arrow) using the latter $\bar{\rho}_{3D}$ as reference. The
 950 uncertainty in both the model and surrogate truth was
 951 set to 3% of the latter, *i.e.*, $f = 0.03$. This estimate
 952 is in line with the absolute calibration accuracy of cur-
 953 rent space borne instruments like MISR [Bruegge *et al.*,
 954 2002] and MERIS [Kneubühler *et al.*, 2002], among oth-
 955 ers. Obviously there is a tendency for those 3-D MC mod-
 956 els that have participated in the computation of $\bar{\rho}_{3D}$ to
 957 have smaller χ^2 values in RAMI-3 than in RAMI-2. This
 958 is particularly so for the heterogeneous BRF simulations,
 959 where **drat**, **FLIGHT**, **Rayspread** and **sprint-3** served as
 960 credible models for all the “floating spheres” test cases.

961 In the homogeneous case, however, both the number and
962 names of the credible 3-D MC models changed from one
963 test case to another. RT models that did not update
964 their BRF simulations in any significant manner during
965 RAMI-3, *e.g.*, `1/2-discret` and `FLIGHT`, do not show any
966 dynamics in their χ^2 values in the depicted graphs. Oth-
967 ers, like the `Sail++` and `RGM` models in the homogeneous
968 case, for example, have reduced the distance between
969 their BRF simulations and $\bar{\rho}_{3D}$ in RAMI-3 which trans-
970 lates into smaller $\chi^2(\text{red})$ and $\chi^2(\text{NIR})$ values when com-
971 pared to those of RAMI-2. `FRT` was the only non Monte
972 Carlo model to participate in the “floating spheres” test
973 cases during both RAMI-2 and RAMI-3. Here one notices
974 a substantial improvement in its $\chi^2(\text{NIR})$ value together
975 with a slight increase in $\chi^2(\text{red})$.

4. New test cases in RAMI-3

976 A series of additional experiments and measurements
977 were proposed for RAMI-3 that address new issues or
978 complement others raised during RAMI-2. In the follow-
979 ing, the results obtained for the “birch stand” canopy will
980 be presented first. Next the “true zoom-in” scene, with
981 its additional measurements, will be revisited before com-
982 paring the BRF simulation results for the “conifer forest”
983 scene with and without topography. Last but not least,
984 results for the “floating spheres” purist corner will also
985 be displayed.

4.1. The birch stand

986 This set of experiments was suggested to simulate the
987 radiative transfer regime in the red and near-infrared
988 spectral bands for spatially heterogeneous scenes resem-
989 bling boreal birch stands (see Figure 9). The $100 \times 100 \text{ m}^2$
990 scene is composed of a large number of non-overlapping
991 tree-like entities of different sizes and spectral proper-
992 ties that are randomly located across (and only partially
993 covering) a planar surface representing the underlying
994 background. Individual tree objects were represented
995 by an ellipsoidal crown located just above a cylindrical
996 trunk. The finite sized foliage was randomly distributed
997 within the ellipsoidal volumes that represented the tree
998 crowns, and was characterized by radiative properties (re-
999 flectance, transmittance) that are typical for birch trees.
1000 Table 3 provides an overview of the structural and spec-
1001 tral properties associated with the 5 tree classes of the
1002 “birch stand” scene.

1003

1004

4.1.1. Canopy-level BRF simulations

1005 Figure 10 presents model generated total BRFs in the
1006 red (left column) and NIR (right column) spectral do-
1007 main corresponding to observations of the “birch stand”
1008 along the principal (upper panels) and orthogonal (lower
1009 panels) planes for illumination conditions of $\theta_i = 20^\circ$ and
1010 $\theta_i = 50^\circ$. It can be seen that most models generate rela-
1011 tively similar BRF patterns with the exception of `5Scale`.
1012 This systematic difference may be partly explained by
1013 the fact that `5Scale` implemented a “birch stand” scene
1014 composed of only one single tree class having structural
1015 and spectral properties that corresponded to the aver-
1016 age characteristics of the 5 tree classes described on the
1017 RAMI website. Moreover, `5Scale`’s multiple scattering
1018 scheme was designed for denser forests than the “birch
1019 stand” scene with a mean LAI of 0.398. The `drat` model
1020 generates BRFs that, in particular in the red spectral do-
1021 main, have a tendency to be somewhat higher than those
1022 of `Dart`, `Rayspread`, `raytran` and `Sprint3`. Further anal-
1023 ysis revealed that these differences arise primarily due

1024 to the single-collided foliage BRF component. One possible
1025 explanation may be found in the exact spatial arrangement
1026 of the various discrete leaf elements that make up the crown
1027 foliage in the `drat` simulations. The commonly used procedure
1028 of “cloning” individual tree objects when generating a larger
1029 canopy scene, may imply that small differences in the leaf
1030 orientations and positions—especially along the rim of the
1031 crown volume—translate into noticeable differences in the
1032 simulated BRF values at the level of the whole scene. These
1033 differences are, however, only detectable due to the increasing
1034 agreement that now exists between the various RT models that
1035 have contributed to RAMI-3. The histograms of model-to-ensemble
1036 BRF differences, δ_m in the “birch stand” scene (central
1037 panels in Figure 10), for example, show that the BRFs
1038 simulated by any one of the models `Dart`, `drat`, `frrt`,
1039 `Rayspread`, `raytran` and `Sprint3` typically fall within
1040 2% of the ensemble average—and this irrespective of the
1041 plane of observation.
1042

1043

1044 4.1.2. Local transmission transects

1045 Since the x, y location of every individual tree in the
1046 “birch stand” scene was specified on the RAMI website a new
1047 measurement type—asking for local transmission measurements
1048 along a transect of 21 adjacent $1 \times 1 \text{ m}^2$ patches—had been
1049 proposed. Models were asked to provide simulation results
1050 quantifying the total (*i.e.*, direct plus diffuse) transmission
1051 of radiation at the level of the background for two transects
1052 located at the center of the birch stand scene with orientations
1053 that were parallel and perpendicular to the azimuthal direction
1054 of the incident radiation, ϕ_i , respectively. This setup, which
1055 aimed at reproducing conditions resembling those encountered
1056 in actual field measurements, was rather demanding on the
1057 capabilities of most RT models. The entire birch stand scene
1058 had to be illuminated but the transmission measurements were
1059 restricted to small adjacent areas in the center of the scene.
1060 This led to only two RT models contributing to this measurement
1061 type (`raytran` and `Sprint3`). Figure 11 shows their local
1062 transmission simulations for transects oriented parallel (left
1063 panels) and perpendicular (right panels) to the direction of
1064 the illumination azimuth (ϕ_i) in both the red (top panels)
1065 and NIR (bottom panels) spectral domain. Although the
1066 simulation results are somewhat different, both models capture
1067 obvious features in the spatial pattern of the local canopy
1068 transmission. The various pink arrows indicate obvious
1069 correlations with predominantly shadowed and illuminated
1070 patches occurring along the transects depicted (in a
1071 perspective-free manner) at the top or bottom of each of
1072 the four graphs. One should also note that both models
1073 occasionally simulate local transmission values that are
1074 larger than unity (*i.e.*, they fall within the grey shaded
1075 area at the top of each graph) which is an unambiguous
1076 signature of the presence of horizontal radiation fluxes. The
1077 occurrence of $T > 1$ is somewhat more frequent in the
1078 NIR due to the larger single-scattering albedo ($\omega_L = r_L + t_L$)
1079 of the foliage there, as well as for transect orientations
1080 that are perpendicular to ϕ_i , which are the ones least
1081 affected by shadows from adjacent tree crowns.
1082
1083
1084

4.2. The true zoom-in experiment

1085 The “true zoom-in” experiment was first proposed during
1086 RAMI-2 (section 2.2 in *Pinty et al.* [2004b]) and consists
1087 of a $270 \times 270 \text{ m}^2$ scene featuring a number of spherical
1088 and cylindrical volumes—having precisely defined locations—
1089 that are filled with disc-shaped scatterers hav-

1090 ing different spectral properties (Table 5 and Figure 2 in
1091 *Pinty et al.* [2004b]). The scene itself is illuminated over
1092 its entire length whilst RT simulations are to be extracted
1093 over a set of progressively smaller target areas located at
1094 the center of the scene. The spatial resolutions of these
1095 target areas are 270, 90 and 30 m, respectively. Such true
1096 zoom-ins are useful when 1) the nature of local horizontal
1097 fluxes—arising from the deterministic occurrence of
1098 gaps and shadows in and immediately around the sam-
1099 pling area—are to be studied/accounted for, and 2) the
1100 creation of artificial “order”, due to cyclic boundary con-
1101 ditions that reproduce the scene *ad infinitum*, has to be
1102 avoided. The latter may arise when RT models have to
1103 be executed on 3-D canopy representations at very high
1104 spatial resolutions since the complexity of the scene is
1105 such that spatially extensive representations cannot be
1106 generated due to computer memory limitations.

1107 Within RAMI-3 the number of local patches in the
1108 “true zoom-in” experiment was extended to nine, such
1109 that the BRF simulations at 90 (30) m spatial resolu-
1110 tion, when averaged over all nine patches equal that of
1111 the (central) patch at the coarser 270 (90) m spatial
1112 resolution since the TOC reference level remained the
1113 same throughout the scene. The necessity for determin-
1114 istic canopy representations and the complexity of the
1115 RT simulation setup was, however, such that only **drat**,
1116 **Sprint-3**, **raytran** and **Rayspread** performed all of these
1117 simulations. Figure 12 thus restricts itself to total BRF
1118 simulations in the principal (top panels) and orthogonal
1119 (bottom panels) viewing planes for the 270 m (left), 90
1120 m (middle) and 30 m (right) patches located at the cen-
1121 ter of the scene (for which also simulations from **DART**
1122 were available). The illumination zenith angle was set
1123 to 20° and the spectral properties of the environment
1124 feature typical NIR conditions. Going from coarse to
1125 fine spatial resolutions (left to right panels in Figure 12)
1126 one notices that the discrepancies between the various
1127 model simulations increase both in the principal and or-
1128 thogonal planes. In particular, it is the **DART** and the
1129 **Sprint3** models that differ from the BRF simulations
1130 of **drat**, **Rayspread** and **raytran**. Possible reasons for
1131 these BRF differences include 1) a magnification of the
1132 impact of small structural differences in the determin-
1133 istic scene setup as the spatial resolution becomes finer,
1134 and/or, 2) the occurrence of different patterns of shadow-
1135 ing/illumination due to erroneously specified illumination
1136 azimuth angles.

1137 4.2.1. Local horizontal flux measurements

1139 In the visible part of the solar spectrum the divergence
1140 of horizontal radiation in vegetation canopies is largely
1141 controlled by the occurrence of mutual shadowing be-
1142 tween individual canopy elements and photon channel-
1143 ing through the gaps between them. As the canopy tar-
1144 get becomes smaller the likelihood of non-zero horizontal
1145 radiation balances increases, resulting in local radiative
1146 regimes that are highly variable across the overall domain
1147 of the canopy [*Widlowski et al.*, 2006b]. The interpreta-
1148 tion, spatial distribution and up-scaling of *in situ* mea-
1149 surements thus could benefit from a quantitative analysis
1150 of the magnitude (and directionality) of horizontal radi-
1151 ation transport, not only because this may contribute
1152 toward the design of optimal sampling schemes for fu-
1153 ture field validation campaigns, but also, because it may
1154 allow the identification of site-specific spatial resolution
1155 thresholds below which the pixel-based interpretation of
1156 remotely sensed data may no longer be adequate (with-
1157 out explicit accounting of horizontal radiation transport).

1158 RAMI-3 therefore introduced a horizontal flux measure-
1159 ment for the “true zoom-in” canopy scene, where par-
1160 ticipants were asked to simulate the total flux [W] that
1161 entered and exited through the various sides of a vir-
1162 tual voxel (box) encompassing the canopy at different
1163 spatial resolutions. These voxels—which coincide both
1164 in size and location with the local areas used for the
1165 “true zoom-in” BRF simulations—extend to a height of
1166 15 m and have their lateral sides either parallel (constant
1167 x coordinate) or perpendicular (constant y coordinate)
1168 with the azimuth of the incident radiation, ϕ_i (see Fig-
1169 ure 13). As was the case for the local transmission tran-
1170 sect measurement, only a couple of models (**Sprint-3**
1171 and **raytran**) submitted results for the local horizontal
1172 flux experiment. Figure 14 displays the results of these
1173 simulations for voxel locations corresponding to the BRF
1174 simulations depicted in Figure 12. More specifically, the
1175 various entering (solid) and exiting (dashed) total hor-
1176 izontal fluxes, normalised by the total incident flux at
1177 the top of the canopy, are shown for voxels with spa-
1178 tial dimensions equal to 270 m (left), 90 m (middle) and
1179 30 m (right) in the NIR spectral domain. The illumina-
1180 tion azimuth, ϕ_i is parallel (perpendicular) to the voxel
1181 sides labeled Y_{LOW} and Y_{HIGH} (X_{LOW} and X_{HIGH}), and
1182 $\theta_i = 20^\circ$.

1183
1184 The direct illumination component entering through
1185 the sunward side of a voxel (X_{HIGH}) and exiting through
1186 its opposite side (X_{LOW}) will naturally increase the mag-
1187 nitude of the corresponding normalised fluxes with re-
1188 spect to fluxes occurring in other directions and through
1189 other lateral sides of the voxel. These latter fluxes, in
1190 turn, can only arise from radiation that has been scat-
1191 tered by the canopy/soil system, and tend to remain
1192 directionally invariant in canopies with randomly dis-
1193 tributed Lambertian scatterers [Widlowski *et al.*, 2006b].
1194 By going from left to right in Figure 14, that is, from
1195 relatively large voxels to smaller ones, it can be seen that
1196 1) the differences between entering and exiting fluxes in-
1197 crease, due to the increasingly non-random (and highly
1198 deterministic) location of shadows and gaps, and 2) the
1199 magnitude of the various horizontal fluxes increases, since
1200 the ratio of the lateral and upper voxel sides increases
1201 also. The total net horizontal flux of these voxels (*i.e.*,
1202 the sum of all 4 laterally entering radiation streams mi-
1203 nus the sum of the 4 laterally exiting radiation streams),
1204 when normalised by the incident total flux at the TOC
1205 level, was found to be of the order of -0.010 (-10^{-4})
1206 at a spatial resolution of 270 m, -0.099 (-0.002) at 90
1207 m, and 0.038 (0.007) at 30 m by the model **Sprint3**
1208 (**raytran**). One should note that **Sprint3** deviates by ~ 1
1209 % from the zero net horizontal radiation transport that
1210 energy conservation dictates at a spatial resolution of 270
1211 m – since here the entire scene is contained within the
1212 voxel. The increasing magnitude of the net lateral radi-
1213 ation exchanges as function of spatial resolution is, how-
1214 ever, confirmed by both models. This behaviour has to
1215 be accounted for when deriving domain-averaged canopy
1216 transmission, absorption or reflectance estimates on the
1217 basis of a series of local point measurements, *e.g.*, Tian
1218 *et al.* [2002]; Gobron *et al.* [2006].

4.3. The conifer forest

1219 The “conifer forest” scene was originally proposed
1220 during RAMI-2 with the aim of simulating the radia-
1221 tive transfer regime in structurally heterogeneous scenes
1222 of rather large spatial extent ($500 \times 500 \text{ m}^2$) that fea-
1223 tured tree architectures and spectral properties reflecting
1224 those of typical coniferous forests (overlying a snow back-

ground). The RAMI-2 specifications of the “conifer forest” included conical tree crown representations (of fixed dimensions) that were distributed uniformly over a Gaussian shaped hill surface. In RAMI-3 a non-topography version of the same coniferous forest was added in order to investigate whether the deviations in the RT simulations in the Gaussian hill scenario were solely due to the topography itself. Both implementations of the “conifer forest” feature identical numbers and sizes of trees. Figure 15 displays the model simulated BRFs in the principal (top 2 rows) and orthogonal (bottom 2 rows) viewing planes for the “conifer forest” scene with topography (left panels), without topography (middle panels), and the difference between these two (right panels). Simulations pertain to the red (top and third row) and near-infrared (second and bottom row) spectral regimes of the canopy, and $\theta_i = 40^\circ$.

One notices the close agreement between the BRF simulations of the models `drat`, `Rayspread`, `raytran`, and `Sprint3` in all of the test cases. The `MAC` model provided identical simulations for both the flat background and the Gaussian hill scenarios. Both of these tend to be higher than the BRF values from most other models, however. The `5Scale` model, which utilises a cylinder and a cone to represent the shape of the tree crowns, generates somewhat higher BRF values in the red spectral domain and somewhat lower BRF values in the NIR spectral domain. Accounting for the reduced number of models participating in the Gaussian hill case, one may say that, overall, the envelope of all the BRF simulations in the Gaussian hill scenario is very similar to that in the flat background case. The impact of topography becomes, however, noticeable when subtracting the BRF simulations in the flat background case from those of the corresponding Gaussian hill scenario (right column) – in particular at large view zenith angles. For observations close to nadir, on the other hand, few topography-induced differences can be observed since both “conifer forest” representations feature identical canopy statistics (*e.g.*, LAI, tree number, fractional cover, *etc.*). In the principal plane the presence of a hill shaped background thus leads to enhanced BRFs in the backward scattering direction (*i.e.*, a large amount of radiation is reflected back from the illuminated slopes of the hill), and reduced BRFs in the forward scattering direction (*i.e.*, little reflection from that part of the scene that lies in the shadow of the hill). In the orthogonal plane, the Gaussian hill BRFs exceed those of the flat background case at large view zenith angles because of the larger contribution from the snowy slopes of the Gaussian hill (*i.e.*, the single-uncollided BRF component). In the NIR, this effect is somewhat dampened by the single-collided and multiple-collided BRF components, which tend to be larger in the flat background case. The absolute impact that the Gaussian hill exerts on the simulated BRFs thus tends to be more noticeable in the red than the NIR spectral regime.

4.4. The “floating spheres” purist corner

Adding conservative scattering conditions in heterogeneous canopy environments allows to push the RT formulations of 3-D models to their limits, in particular with respect to the multiple scattered radiation component. RAMI-3 thus proposed to run the “floating spheres” test cases under purist corner conditions, *i.e.*, with $r_l = t_l = 0.5$ and $\alpha = 1$. Seven RT models participated in these test cases and their simulation results are shown in Figure 16. More specifically, the total BRFs in the principal (left columns) and orthogonal (right columns) planes for discrete (top row) and turbid medium (bottom row)

1292 “floating spheres” representations at two different illu-
1293 mination zenith angles ($\theta_i = 20^\circ$ and 50°) under purist
1294 corner conditions are shown. The structure of the scenes
1295 is indicated in the inlaid images. One can see that, simi-
1296 lar to the solar domain simulations, the 3-D Monte Carlo
1297 models `drat`, `Rayspread`, `raytran`, and `Sprint3` gener-
1298 ated very similar results, with both DART and FRT being
1299 somewhat different in the turbid and discrete cases. The
1300 `4SAIL2` model, on the other hand, generates significantly
1301 higher BRFs than the other models.

4.5. Overall model performances in RAMI-3

1302 There is an expectation that the RAMI activity should
1303 provide an overall indication of the performance of a
1304 given model. This is, however, not a trivial task,
1305 since there is a need to account for the reliability of
1306 the model simulations, the number of experiments per-
1307 formed, and the computer processing time that was re-
1308 quired to do these simulations. Instead, Figure 17 pro-
1309 vides an overview of the participation and model-to-
1310 ensemble performance of the various models that con-
1311 tributed toward RAMI-3. Statistics are provided for to-
1312 tal BRF simulations over structurally homogeneous (top
1313 table) and heterogeneous (bottom table) discrete canopy
1314 representations. The various model names are listed on
1315 the top of each table (one per column). The experiment
1316 identifier is provided to the left, whereas the spectral
1317 regime is indicated to the right of each table column.
1318 Light (dark) grey fields indicate incomplete (no) data
1319 submission. The green-yellow-red colour scheme repre-
1320 sents the overall model-to-ensemble difference, $\bar{\delta}_m$ quan-
1321 tifying the dispersion that exists between a given model
1322 m and all other models that have performed the complete
1323 set of prescribed total BRF simulations for the experi-
1324 ment/spectral regime combination of interest. One will
1325 note that almost all models—whether analytic, stochas-
1326 tic, hybrid, or Monte Carlo—agree to within 2–4 % with
1327 the ensemble of all other models in the homogeneous
1328 cases. The MBRF model stands out as being somewhat
1329 different from the other RAMI-3 participants. In the
1330 heterogeneous case, the 3-D MC models tend to be in
1331 good agreement with the ensemble of model simulations,
1332 whereas models with structural and radiative approxima-
1333 tions/parameterisation deviate somewhat more - as was
1334 discussed and documented in the various previous sub-
1335 sections. One should note that the predominant hue in
1336 the $\bar{\delta}_m$ colours of any given row in Figure 17 depends
1337 both on the degree and manner in which the models are
1338 dispersed around the main cluster of simulation results.
1339 The mostly red colours characterising $\bar{\delta}_m$ for the discrete
1340 “floating spheres” canopies in the NIR spectral domain
1341 (second last row in lower panel), for example, are due
1342 to the consistently large deviations of the `5Scale` and
1343 `4SAIL2` simulations with respect to each other and to the
1344 cluster of 3D Monte Carlo models. Finally, the large,
1345 noticeable, amount of (light and dark) grey patches in
1346 Figure 17 indicate that a significant number of experi-
1347 ments were not completed or submitted.

5. Concluding remarks

1348 The third phase of the Radiation transfer Model In-
1349 tercomparison (RAMI) activity with its record participa-
1350 tion, its extensive set of new experiments and measure-
1351 ments, and its substantially improved agreement between
1352 3-D MC models sets a milestone in the evolution of the
1353 RT modelling community. It is now estimated that about
1354 60 - 65% of all currently existing canopy reflectance mod-

1355 els have voluntarily participated at some time or other in
1356 the RAMI initiative. Through its continuing support and
1357 active encouragement of RAMI the RT modelling com-
1358 munity has demonstrated maturity 1) by acknowledging
1359 the necessity for quality assured RT models if these are
1360 to be applied to the interpretation of remotely sensed
1361 data, 2) by voluntarily contributing to the establishment
1362 of benchmarking scenarios against which future develop-
1363 ments of RT models may be evaluated, and 3) by agree-
1364 ing to publish their model simulations in the refereed
1365 scientific literature prior to knowing the results of the
1366 intercomparison exercise. Since its first phase in 1999,
1367 RAMI has served as a vehicle to document the perfor-
1368 mance of the latest generation of RT models by charting
1369 both their capabilities and weaknesses under a variety
1370 of spectral and structural conditions. During RAMI-3 it
1371 has been possible to actually demonstrate, for the first
1372 time, a general convergence of the ensemble of submitted
1373 RT simulations (with respect to RAMI-2), and to doc-
1374 ument the unprecedented level of agreement that now
1375 exists between the participating 3-D Monte Carlo mod-
1376 els. These positive developments do not only further the
1377 confidence that may be placed in the quality of canopy
1378 reflectance models, but they also pave the way for ad-
1379 dressing new and challenging issues, most notably, in the
1380 context of supporting field validation efforts of remotely
1381 sensed products. The latter is of prime importance given
1382 the abundance of global surface products from the cur-
1383 rent fleet of instruments, like MISR, MODIS, MERIS,
1384 *etc.* The usage of quality-assured RT models in detailed
1385 simulations of *in situ* field measurements at very high
1386 spatial resolutions is thus only a first step toward propos-
1387 ing optimal sampling/up-scaling schemes that guarantee
1388 accurate domain-averaged absorption, transmission, *etc.*
1389 estimates. RAMI-3 has, however, also shown that only a
1390 few models are currently able to perform such kinds of RT
1391 simulations. The challenge thus lies with the modelling
1392 community as a whole to provide the scientists involved
1393 in field validation campaigns of satellite derived surface
1394 products with optimal sampling practices that are rooted
1395 in a proper understanding of the radiative transfer in ar-
1396 chitecturally complex 3-D media.

1397

5.1. Structurally divergent model premises

1398 More models than ever participated in the third phase
1399 of RAMI, and the agreement between them, in particu-
1400 lar for the various baseline scenarios, has noticeably in-
1401 creased with respect to previous phases of RAMI (Fig-
1402 ure 7). The continuation of the strategy adopted during
1403 RAMI-2, *i.e.*, to provide detailed descriptions of the posi-
1404 tion and orientation of every single leaf in scenes with dis-
1405 crete foliage representations, as well as indications of all
1406 tree/crown locations in the relevant scenes on the RAMI
1407 website, has—among other factors—contributed to im-
1408 proving the agreement among the various 3-D MC RT
1409 models (Figures 6, 8, 10, 16 and Table 2). This devel-
1410 opment provides further weight to using these models in
1411 defining a “surrogate truth” that may then be used—even
1412 for structurally heterogeneous canopy architectures—to
1413 obtain an indication of the performance of other RT mod-
1414 els. It may be argued, however, that such an approach
1415 is only meaningful if all the models implement identical
1416 canopy representations in their RT simulations. Both
1417 the deviations in the structural premises of a RT model
1418 and the approximations and/or errors in the implementa-
1419 tion of the model’s radiative transfer formulation may be
1420 held responsible for the observed BRF/flux differences.
1421 If the purpose of RAMI were solely to identify RT re-

1422 lated differences in canopy reflectance models, then the
1423 current flexibility in the implementation of RAMI test
1424 cases would have to be replaced by rigorously specified
1425 canopy architectures that were specifically tailored to the
1426 scene description formalism of each and every partici-
1427 pating RT model. Alternatively, the derivation and use
1428 of “effective” state variables may be proposed to poten-
1429 tial RAMI participants, since recent findings, *e.g.*, *Cairns*
1430 *et al.* [2000]; *Pinty et al.* [2006]; *Widlowski et al.* [2005],
1431 have suggested that diverging target structures may still
1432 yield identical radiative properties provided that “effec-
1433 tive” instead of actual state variable values are avail-
1434 able for RT simulations (one possible approach to derive
1435 such effective state variables is described in *Pinty et al.*
1436 [2004a]).

1437
1438 Ultimately, however, it is the accuracy of the retrieved
1439 state variable values that counts in RT model applica-
1440 tions. The logical consequence of this line of reasoning
1441 thus would be to address the inversion of RT models
1442 in the context of RAMI against predefined sets of spec-
1443 tral and angular observations, similar to those provided
1444 by the current fleet of space borne sensors, *e.g.*, ATSR-
1445 2/AATSR [*Stricker et al.*, 1995], CHRIS-Proba [*Barnsley*
1446 *et al.*, 2004], MISR [*Diner et al.*, 2002], and POLDER
1447 [*Deschamps et al.*, 1994]. In this way, the impact that
1448 the various structural and radiative formalisms in the
1449 RT models may have with respect to the values of the re-
1450 trieved state variables could then be assessed in the light
1451 of the known uncertainties in the available surface BRFs.
1452 Indeed, during RAMI-1 a set of “inverse mode” scenar-
1453 ios had been proposed but this had been abandoned in
1454 subsequent phases due to a lack of participants. Given
1455 the close agreement of the various participating models in
1456 RAMI-3, it may become appropriate to revisit this issue
1457 in the future.

5.2. The RAMI On-line model checker (ROMC)

1458 One of the positive outcome of RAMI-3 is the consis-
1459 tently good agreement (see Table 2) between simulation
1460 results of a small set of 3-D MC models – and this both
1461 over homogeneous as well as heterogeneous vegetation
1462 canopies. It thus is feasible to derive a “surrogate truth”
1463 for almost all of the measurements and experiments fea-
1464 tured within RAMI (current exceptions are the “local
1465 transmission transects”, the “local horizontal fluxes” and
1466 some of the BRF simulations relating to the 30 m spa-
1467 tial resolution patches in the “true zoom-in” experiment).
1468 With this valuable dataset at hand, it becomes possible
1469 to allow model owners, developers and customers to evalu-
1470 ate the performance of a given RT model even outside
1471 the frame of a RAMI phase. To facilitate such an under-
1472 taking the RAMI On-line Model Checker (ROMC) was
1473 developed at the Joint Research Centre of the European
1474 Commission in Ispra, Italy. The ROMC is a web-based
1475 interface allowing for the on-line evaluation of RT mod-
1476 els using as reference the “surrogate truth” derived from
1477 among the 6 Monte Carlo models **DART**, **drat**, **FLIGHT**,
1478 **Rayspread**, **raytran** and **Sprint3** using an appropriate
1479 set of selection criteria (see section 3.3.3). Access to
1480 the ROMC can be obtained either via the RAMI web-
1481 site or directly using the URL <http://romc.jrc.it/>⁴.
1482 After providing a username and valid email address, the
1483 ROMC can be utilised in two different ways: 1) in **debug**
1484 **mode**, which allows to *repeatedly* compare the output of
1485 a RT model to that of one or more experiments and/or
1486 measurements from RAMI, *i.e.*, the simulation results
1487 are available on the RAMI website, and 2) in **validate**
1488 **mode**, which enables the *once-only* testing of the RT

1489 model against a continuously changing set of test cases
1490 that are similar but not quite equivalent to those from
1491 RAMI, *i.e.*, the solutions are not known *a priori* and the
1492 experiments cannot be repeated.

1493

1494 • In **debug mode** users may choose to execute one
1495 particular experiment and/or measurement from the set
1496 of RAMI-3 test cases *ad infinitum*, or, at least until they
1497 are satisfied with the performance of their model. De-
1498 tailed descriptions of the structural, spectral, illumina-
1499 tion and measurement conditions are available. Once the
1500 model simulation results are generated, they can be up-
1501 loaded via the web-interface, and—provided they adhere
1502 to the RAMI filenames and formatting conventions—
1503 this process will result in a series of graphical results files
1504 being made available for all test cases. In debug mode
1505 users may not only download their ROMC results but
1506 also an ASCII file containing the actual “surrogate truth”
1507 data.

1508 • In **validate mode** users may choose between
1509 structurally homogeneous and/or heterogeneous “float-
1510 ing spheres” canopies to verify the performance of their
1511 model. The actual set of test cases will, however, be
1512 drawn randomly from a large list of possible ones, such
1513 that it is unlikely to obtain the same test case twice,
1514 *i.e.*, in all likelihood one will not “know” the solution
1515 *a priori*. Again, the “surrogate truth” was derived from
1516 simulations generated by models belonging to the same
1517 set of 3-D MC models as was the case for the debug
1518 mode. In validate mode the reference data will, however,
1519 not be available for downloading. The procedure for data
1520 submission, on the other hand, is identical to that of the
1521 debug mode, and—provided that all RAMI formatting
1522 and filenames requirements were applied—will also lead
1523 to a results page featuring a variety of intercomparison
1524 graphics.

1525

1526 Users may download their ROMC results either as jpeg
1527 formatted images from the ROMC website, or else, opt
1528 for receiving them via email in postscript form. Both
1529 the debug and validate mode ROMC results files feature
1530 a reference number and a watermark. Available graphs
1531 include: Plots of both the model and reference BRFs
1532 in the principal or orthogonal plane, 1 to 1 plots of the
1533 model and reference BRFs, histograms of the deviations
1534 between model and reference BRFs, χ^2 graphs for all sub-
1535 mitted measurements using an f value of 3% as well as,
1536 graphs depicting the deviation of the model and reference
1537 fluxes using barcharts. Users of ROMC are encouraged
1538 to utilise only ROMC results that were obtained in val-
1539 idate mode for publications. Those obtained in debug
1540 mode, obviously, do not qualify as proof regarding the
1541 performance of a RT model since all simulation results
1542 may readily be viewed on the RAMI website. Last but
1543 not least, a large ensemble of FAQs should help to guide
1544 the user through the ROMC applications. It is hoped
1545 that the ROMC will prove useful for the RT modelling
1546 community, not only by providing a convenient means to
1547 evaluate RT models outside the triennial phases of RAMI
1548 (something that was rather tedious in the past if authors
1549 wished to rely on the experiences gained from RAMI,
1550 *e.g.*, *Gastellu-Etcheberry et al.* [2004]) but also to attract
1551 participation in future RAMI activities.

1552

5.3. Future perspectives for RAMI

1553 RAMI was conceived as an open-access community ex-
1554 ercise and will continue to pursue that direction. As such

1555 it's goal is to move forward in a manner that addresses
1556 the needs of the majority of RT model (developers and
1557 users). For example, relatively simple RT modelling ap-
1558 proaches designed only to simulate integrated fluxes, like
1559 the **2-Stream** model, should not be neglected in future
1560 developments of RAMI due the large communities in-
1561 volved with soil-vegetation-atmosphere transfer (SVAT)
1562 models, as well as general circulation models. Whereas
1563 such two stream approaches remove all dependencies on
1564 vegetation structure beyond leaf quantity and orienta-
1565 tion, the various findings of RAMI-3, and in particular
1566 the above discussion, have highlighted the relevance of
1567 canopy structure in forward mode RT simulations. With
1568 every model having its own implementation of "reality" it
1569 may be appropriate to provide as detailed descriptions as
1570 possible of highly realistic canopy architectures in future
1571 phases of RAMI (see for example *Disney et al.* [2006]).
1572 Various techniques are currently available for the genera-
1573 tion of realistic 3-D trees, the most well known one being
1574 probably the L-systems approach, *e.g.*, *Prusinkiewicz and*
1575 *Lindenmayer* [1990]; *Weber and Penn* [1995]; *De Reffye*
1576 *and Houllier* [1997]. Using these methodologies to gener-
1577 ate a detailed depiction of the architectural character-
1578 istics of (part of) well documented sites—like BOREAS
1579 [*Sellers et al.*, 1997] and/or the Kalahari transect (SA-
1580 FARI 2000) [*Scholes et al.*, 2004], for example—would
1581 allow to 1) study the variability in the radiative surface
1582 properties predicted by a whole suite of participating RT
1583 models, as well as their possible impact on the hydro-
1584 logical and carbon cycles, 2) investigate by how much
1585 RT model simulations vary when carried out on the basis
1586 of canopy representations with a progressively increasing
1587 degree of structural abstractions (all state variable val-
1588 ues remain constant, or are converted to "effective" val-
1589 ues), *e.g.*, *Smolander and Stenberg* [2005]; *Rochdi et al.*
1590 [2006], 3) compare such surface BRF simulations with
1591 atmospherically-corrected observations from space borne
1592 instruments, 4) investigate the potential of RT models
1593 to reproduce *in situ* measurements of transmitted light,
1594 *e.g.*, Tracing Radiation and Architecture of Canopies
1595 (TRAC) instrument [*Chen and Cihlar*, 1995; *Leblanc*,
1596 2002], and/or hemispherical photographs [*Leblanc et al.*,
1597 2005; *Jonckheere et al.*, 2005], and 5) assess the accuracy
1598 of up-scaling methodologies currently used in validation
1599 efforts of satellite derived products like FAPAR and LAI,
1600 *e.g.*, *Morisette et al.* [2006]. In this way RAMI can ac-
1601 tively contribute towards systematic validation efforts of
1602 RT models, operational algorithms, and field instruments
1603 – as promoted by the Committee on Earth Observation
1604 Satellites (CEOS).

1605 **Acknowledgments.** The definition of the RAMI test
1606 cases on a dedicated website, the coordination of the RAMI
1607 participants, and the analysis of the submitted simulation re-
1608 sults would not have been possible without the financial sup-
1609 port of the European Commission, and more specifically, the
1610 Global Environment Monitoring unit of the Institute for Envi-
1611 ronment and Sustainability in the DG Joint Research Centre.
1612 The valuable comments of the three anonymous reviewers and
1613 the stimulating exchanges with the various scientists of the
1614 RAMI Advisory Body (RAB), as well as those involved with
1615 the I3RC, are also gratefully acknowledged.

Notes

1. Due to the renaming of all European Commission web-
sites this URL is likely to change in the near future to
<http://rami-benchmark.jrc.ec.europa.eu/>

2. Canopy structure is defined here as the (statistical or deterministic) description of locations and orientations of foliage and woody constituents within the three-dimensional space of a RAMI scene.
3. Due to the renaming of all European Commission websites this URL is likely to change in the near future to <http://romc.jrc.ec.europa.eu/> .
4. See footnote 3.

References

References

- 1621 Barnsley, M. J., J. J. Settle, M. Cutter, D. Lobb, and
1622 F. Teston, The PROBA/CHRIS mission: a low-cost small-
1623 sat for hyperspectral, multi-angle, observations of the Earth
1624 surface and atmosphere, *IEEE Transactions on Geoscience
1625 and Remote Sensing*, 42, 1512–1520, 2004.
- 1626 Bruegge, C. J., N. L. Chrien, R. R. Ando, D. J. Diner, W. A.
1627 Abdou, M. C. Helmlinger, S. H. Pilorz, and K. J. Thome,
1628 Early validation of the Multi-angle Imaging SpectroRa-
1629 diometer (ISR) radiometric scale, *IEEE Transactions on
1630 Geoscience and Remote Sensing*, 40, 1477–1492, 2002.
- 1631 Bunnik, N. J. J., The multispectral reflectance of shortwave
1632 radiation of agricultural crops in relation with their mor-
1633 phological and optical properties, *Tech. rep.*, Mededelin-
1634 gen Landbouwhogeschool, Wageningen, The Netherlands,
1635 1978.
- 1636 Cahalan, R. F., L. Oreopoulos, A. Marshak, K. F. Evans, A. B.
1637 Davis, R. Pincus, K. Yetzer, B. Mayer, R. Davies, T. Ack-
1638 erman, H. Barker, E. Clothiaux, R. Ellingson, M. Garay,
1639 E. Kassianov, S. Kinne, A. Macke, W. OHirok, P. Partain,
1640 S. Prigarin, A. Rublev, G. Stephens, F. Szczap, E. Takara,
1641 T. Vrnai, G. Wen, and T. Zhuravleva, The international
1642 intercomparison of 3D radiation codes (I3RC): Bringing to-
1643 gether the most advanced radiative transfer tools for cloudy
1644 atmospheres, *Bulletin of the American Meteorological So-
1645 ciety*, 86, 1275–1293, 2005.
- 1646 Cairns, B., A. Lacis, and B. Carlson, Absorption within inho-
1647 mogeneous clouds and its parameterization in general cir-
1648 culation models, *Journal of the Atmospheric Sciences*, 57,
1649 700–714, 2000.
- 1650 Campbell, G. S., Derivation of an angle density function for
1651 canopies with ellipsoidal leaf angle distribution, *Agricul-
1652 tural and Forest Meteorology*, 49, 173–176, 1990.
- 1653 Chen, J. M., and J. Cihlar, Plant canopy gap size analysis the-
1654 ory for improving optical measurements of leaf area index,
1655 *Applied Optics*, 34, 6211–6222, 1995.
- 1656 Chen, J. M., J. Liu, S. G. Leblanc, R. Lacaze, and J. L.
1657 Roujean, Multi-angular optical remote sensing for assess-
1658 ing vegetation structure and carbon absorption, *Remote
1659 Sensing Environment*, 84, 516–525, 2003.
- 1660 Chopping, M. J., A. Rango, K. M. Havstad, F. R. Schiebe,
1661 J. C. Ritchie, T. J. Schmutge, A. N. French, L. Su, L. Mc-
1662 Kee, and R. Davis, Canopy attributes of desert grasslands
1663 and transition communities derived from multi-angular air-
1664 borne imagery, *Remote Sensing Environment*, 85, 339–354,
1665 2003.
- 1666 De Reffye, P., and F. Houllier, Modelling plant growth and
1667 architecture: Some recent advances and applications to
1668 agronomy and forestry, *Current Science*, 73, 984–992, 1997.
- 1669 Deschamps, P. Y., F.-M. Bréon, M. Leroy, A. Podaire,
1670 A. Bricaud, J.-C. Buriez, and G. Sèze, The POLDER mis-
1671 sion: Instruments characteristics and scientific objectives,
1672 *IEEE Transactions on Geosciences and Remote Sensing*,
1673 32, 586–615, 1994.
- 1674 Diner, D. J., J. C. Beckert, G. W. Bothwell, and J. I. Ro-
1675 drigues, Performance of the MISR instrument during its
1676 first 20 months in Earth orbit, *IEEE Transactions on Geo-
1677 science and Remote Sensing*, 40, 1449–1466, 2002.
- 1678 Dirmeyer, P. A., A. J. Dolman, and N. Sato, The global soil
1679 wetness project: A pilot project for global land surface
1680 modeling and validation, *Bulletin of the American Meeo-
1681 rological Society*, 80, 851–878, 1999.
- 1682 Disney, M. I., P. Lewis, and P. R. J. North, Monte Carlo
1683 raytracing in optical canopy reflectance modelling, *Remote
1684 Sensing Reviews*, 18, 163–196, 2000.
- 1685 Disney, M. I., P. Lewis, and P. Saich, 3D modelling of for-
1686 est canopy structure for remote sensing simulations in the
1687 optical and microwave domains, *Remote Sensing of Envi-
1688 ronment*, 100, 114–132, 2006.

1689 Fernandes, R. A., L. S. G., and S. A., A multi-scale analyti-
1690 cal canopy (MAC) reflectance model based on the angular
1691 second order gap size distribution, in *Proceedings of the*
1692 *international geoscience and remote sensing symposium*,
1693 vol. 7, pp. 4431–4433, 2003.

1694 Gastellu-Etchegorry, J.-P., V. Demarez, V. Pinel, and
1695 F. Zagolski, Modeling radiative transfer in heterogeneous
1696 3-d vegetation canopies, *Remote Sensing of Environment*,
1697 58, 131–156, 1996.

1698 Gastellu-Etchegorry, J.-P., E. Martin, and F. Gascon, Dart:
1699 a 3D model for simulating satellite images and studying
1700 surface radiation budget, *International Journal of Remote*
1701 *Sensing*, 25, 73–96, 2004.

1702 Gates, W. L., J. Boyle, C. Covey, C. Dease, C. Doutriaux,
1703 R. Drach, M. Fiorino, P. Gleckler, J. Hnilo, S. Marlais,
1704 T. Phillips, G. Potter, B. Santer, K. Sperber, K. Taylor,
1705 and D. Williams, An overview of the results of the atmo-
1706 spheric model intercomparison project (AMIP I), *Bulletin*
1707 *of the American Meteorological Society*, 73, 1962–1970,
1708 1998.

1709 Gerard, F. F., and P. R. J. North, Analyzing the effect of struc-
1710 tural variability and canopy gaps on forest BRDF using a
1711 geometric-optical model, *Remote Sensing of Environment*,
1712 62, 46–62, 1997.

1713 Gerstl, S. A. W., Angular reflectance signature of the canopy
1714 hotspot in the optical regime, in *4th Intl. Coll. On Spectral*
1715 *Signatures of Objects in Remote Sensing, Aussois, France*,
1716 p. 129, ESA report SP-287, 1988.

1717 Gobron, N., B. Pinty, M. M. Verstraete, and Y. Govaerts, A
1718 semi-discrete model for the scattering of light by vegetation,
1719 *Journal of Geophysical Research*, 102, 9431–9446, 1997.

1720 Gobron, N., B. Pinty, O. Aussedat, J. M. Chen, W. B. Co-
1721 hen, R. Fensholt, V. Gond, K. F. Huemmrich, T. Lavergne,
1722 F. Mélin, J. L. Privette, I. Sandholt, M. Taberner, D. P.
1723 Turner, M. M. Verstraete, and J.-L. Widlowski, Evaluation
1724 of FAPAR products for different canopy radiation trans-
1725 fer regimes: Methodology and results using JRC prod-
1726 ucts derived from SeaWiFS against ground-based estima-
1727 tions, *Journal of Geophysical Research*, 111, D13100, doi:
1728 10.1029/2005/JD006511, 2006.

1729 Goel, N. S., and D. E. Strelbel, Simple beta distribution repre-
1730 sentation of leaf orientation in vegetation canopies, *Agron-*
1731 *omy Journal*, 76, 800–803, 1984.

1732 Govaerts, Y., and M. M. Verstraete, Raytran: A Monte Carlo
1733 ray tracing model to compute light scattering in three-
1734 dimensional heterogeneous media, *IEEE Transactions on*
1735 *Geoscience and Remote Sensing*, 36, 493–505, 1998.

1736 Helbert, J., B. Berthelot, and C. Soler, Hyemalis: Un
1737 simulateur d’images de paysages tridimensionnels com-
1738 plexes, in *Revue Française de Photogrammétrie et de*
1739 *Télétection*, 173 / 174, pp. 27–35, Société Française de
1740 Photogrammétrie et de Télétection, 2003.

1741 Henderson-Sellers, A., A. J. Pitman, P. K. Love, P. Iranne-
1742 jad, and T. Chen, The project for intercomparison of land
1743 surface parameterisation schemes (PILPS): Phases 2 and 3.,
1744 *Bulletin of the American Meteorological Society*, 76, 489–
1745 503, 1995.

1746 Jonckheere, I., B. Muys, and P. Coppin, Assessment of auto-
1747 matic gap fraction estimation of forests from digital hemi-
1748 spheric photography, *Agricultural and Forest Meteorol-*
1749 *ogy*, 132, 96–114, 2005.

1750 Kneubühler, M., M. Schaepman, K. Thome, F. Baret, and
1751 A. Müller, Calibration and validation of Envisat MERIS.
1752 Part 1: vicarious calibration at Rail Road valley Playa
1753 (NV), in *Proceedings of MERIS level 2 validation Work-*
1754 *shop, ESRIN, Frascati, Italy, December 9–13, 2002*.

1755 Kuusk, A., The hot spot effect in plant canopy reflectance, in
1756 *Photon-Vegetation Interactions*, edited by R. Myneni and
1757 J. Ross, pp. 139–159, Springer-Verlag, New York, 1991.

1758 Kuusk, A., A two-layer canopy reflectance model, *Journal of*
1759 *Quantitative Spectroscopy and Radiative Transfer*, 71, 1–9,
1760 2001.

1761 Kuusk, A., and T. Nilson, A directional multispectral forest re-
1762 flectance model, *Remote Sensing of Environment*, 72, 244–
1763 252, 2000.

1764 Latif, M., K. Sperber, J. Arblaster, P. Braconnot, D. Chen,
1765 A. Colman, U. Cubasch, M. Davey, P. Delecluse, D. De-

1766 Witt, L. Fairhead, G. Flato, T. Hogan, M. Ji, M. Kimoto,
1767 A. Kitoh, T. Knutson, H. Le Treut, T. Li, S. Manabe,
1768 O. Marti, C. Mechoso, G. Meehl, S. Power, E. Roeckner,
1769 J. Sirven, L. Terray, A. Vintzileos, R. Voß, B. Wang,
1770 W. Washington, I. Yoshikawa, J. Yu, and S. Zebiak, ENSIP:
1771 The El Niño simulation intercomparison project, *Climate*
1772 *Dynamics*, 18, 255–276, 2001.

1773 Leblanc, S. G., Correction to the plant canopy gap size analy-
1774 sis theory used by the Tracing Radiation and Architecture
1775 of Canopies (TRAC) instrument, *Applied Optics*, 31, 7667–
1776 7670, 2002.

1777 Leblanc, S. G., and J. M. Chen, A windows graphic user in-
1778 terface (GUI) for the five-scale model for fast BRDF simu-
1779 lations, *Remote Sensing Reviews*, 19, 293–305, 2001.

1780 Leblanc, S. G., J. M. Chen, R. Fernandes, D. W. Deering, and
1781 A. Conley, Methodology comparison for canopy structure
1782 parameters extraction from digital hemispherical photogra-
1783 phy in boreal forests, *Agricultural and Forest Meteorology*,
1784 129, 187–207, 2005.

1785 Lewis, P., Three-dimensional plant modelling for remote sens-
1786 ing simulation studies using the botanical plant modelling
1787 system, *Agronomie - Agriculture and Environment*, 19,
1788 185–210, 1999.

1789 Lovell, J. L., and R. D. Graetz, Analysis of POLDER-ADEOS
1790 data for the Australian continent: the relationship between
1791 BRDF and vegetation structure, *International Journal of*
1792 *Remote Sensing*, 23, 2767–2796, 2002.

1793 Morisette, J. T., F. Baret, J. L. Privette, R. B. Myneni,
1794 J. Nickeson, S. Garrigue, N. Shabanov, M. Weiss, R. Fer-
1795 nandes, S. Leblanc, M. Kalacska, G. A. Sánchez-Azofeifa,
1796 M. Chubey, B. Rivard, P. Stenberg, M. Rautiainen,
1797 P. Voipio, T. Manninen, A. Pilant, T. Lewis, J. James,
1798 R. Colombo, M. Meroni, L. Busetto, W. Cohen, D. Turner,
1799 E. D. Warner, G. W. Petersen, G. Seufert, and R. Cook,
1800 Validation of global moderate resolution LAI products: a
1801 framework proposed within the CEOS Land Product Val-
1802 idation subgroup, *IEEE Transactions on Geoscience and*
1803 *Remote Sensing*, 44, 1804–1817, 2006.

1804 North, P. R. J., Three-dimensional forest light interaction
1805 model using a Monte Carlo method, *IEEE Transactions*
1806 *on Geoscience and Remote Sensing*, 34, 946–956, 1996.

1807 Oreskes, N., K. Shrader-Frechette, and K. Belitz, Verification,
1808 validation, and confirmation of numerical models in the
1809 earth sciences, *Science*, 263, 641–646, 1994.

1810 Pinty, B., N. Gobron, J.-L. Widlowski, S. A. W. Gerstl,
1811 M. M. Verstraete, M. Antunes, C. Bacour, F. Gascon, J.-
1812 P. Gastellu, N. Goel, S. Jacquemoud, P. North, W. Qin,
1813 and R. Thompson, The RAdiation transfer Model Inter-
1814 comparison (RAMI) exercise, *Journal of Geophysical Re-*
1815 *search*, 106, 11,937–11,956, 2001.

1816 Pinty, B., N. Gobron, J.-L. Widlowski, T. Lavergne, and M. M.
1817 Verstraete, Synergy between 1-D and 3-D radiation trans-
1818 fer models to retrieve vegetation canopy properties from re-
1819 mote sensing data, *Journal of Geophysical Research*, 109,
1820 D21205, doi:10.1029/2004JD005214, 2004a.

1821 Pinty, B., J.-L. Widlowski, M. Taberner, N. Gobron, M. M.
1822 Verstraete, M. Disney, F. Gascon, J.-P. Gastellu, L. Jiang,
1823 A. Kuusk, P. Lewis, X. Li, W. Ni-Meister, T. Nilson,
1824 P. North, W. Qin, L. Su, R. Tang, R. Thompson, W. Ver-
1825 hoef, H. Wang, J. Wang, G. Yan, and H. Zang, The RA-
1826 diation transfer Model Intercomparison (RAMI) exercise:
1827 Results from the second phase, *Journal of Geophysical Re-*
1828 *search*, 109, D06210, doi:10.1029/2004JD004252, 2004b.

1829 Pinty, B., T. Lavergne, R. E. Dickinson, J.-L. Wid-
1830 lowski, N. Gobron, and M. M. Verstraete, Simplifying
1831 the interaction of land surfaces with radiation for re-
1832 lating remote sensing products to climate models, *Jour-*
1833 *nal of Geophysical Research*, 111(D02116), D02,116,
1834 doi:10.1029/2005JD005,952, 2006.

1835 Prusinkiewicz, P., and A. Lindenmayer, *The Algorithmic*
1836 *Beauty of Plants*, 240 pp., Springer Verlag, New York, 1990.

1837 Qin, W., and S. A. W. Gerstl, 3-D scene modeling of semi-
1838 desert vegetation cover and its radiation regime, *Remote*
1839 *Sensing of Environment*, 74, 145–162, 2000.

1840 Qin, W., and Y. Xiang, An analytical model for bidirectional
1841 reflectance factor of multicomponent vegetation canopies,
1842 *Science in China (Series C)*, 40, 305–315, 1997.

1843 Rangasayi, H. N., D. Crisp, S. E. Schwartz, G. P. Anderson,
1844 A. Berk, B. Bonnel, O. Boucher, F.-L. Chang, M.-D. Chou,
1845 E. E. Clothiaux, P. Dubuisson, B. Fomin, Y. Fouquart,
1846 S. Freidenreich, C. Gautier, S. Kato, I. Laszlo, Z. Li,
1847 J. H. Mather, A. Plana-Fattori, V. Ramaswamy, P. Ric-
1848 chiazzi, Y. Shiren, A. Trishchenko, and W. Wiscombe, In-
1849 tercomparison of shortwave radiative transfer codes and
1850 measurements, *Journal of Geophysical Research*, 110, doi:
1851 10.1029/2004JD005293, 2005.

1852 Rautiainen, M., P. Stenberg, N. T., and A. Kuusk, The ef-
1853 fect of crown shape on the reflectance of coniferous stands,
1854 *Remote Sensing of Environment*, 89, 41–52, 2003.

1855 Rochdi, N., R. Fernandes, and M. Chelle, An assessment of
1856 needles clumping within shoots when modeling radiative
1857 transfer within homogeneous canopies, *Remote Sensing of*
1858 *Environment*, 102, 116–135, 2006.

1859 Ross, J., *The Radiation Regime and Architecture of Plant*
1860 *Stands*, Dr. W. Junk, Boston, 1981.

1861 Saich, P., P. Lewis, M. Disney, and G. Thackrah, Comparison
1862 of Hymap/E-SAR data with models for optical reflectance
1863 and microwave scattering from vegetation canopies, in *Pro-*
1864 *ceedings of Third International Workshop on Retrieval of*
1865 *Bio- and Geo-Physical Parameters from SAR data for*
1866 *Land Applications*, p. 427, 2001.

1867 Scholes, R. J., P. G. H. Frost, and Y. Tian, Canopy structure
1868 in savannas along a moisture gradient on Kalahari sands,
1869 *Global Change Biology*, 10, 292–302, doi:10.1111, 2004.

1870 Sellers, P. J., F. G. Hall, R. Kelly, A. Black, D. Baldocchi,
1871 J. Berry, M. Ryan, K. J. Ranson, P. M. Crill, D. P. Let-
1872 tenmaier, H. Margolis, J. Cihlar, J. Newcomer, D. Fitzjar-
1873 rald, P. G. Jarvis, S. T. Gower, D. Halliwell, D. Williams,
1874 B. Goodison, D. E. Wickland, and F. E. Guertin, BOREAS
1875 in 1997: Experiment overview, scientific results and future
1876 directions, *Journal of Geophysical Research*, 102, 28,731–
1877 28,770, 1997.

1878 Shultis, J. K., and R. B. Myneni, Radiative transfer in vegeta-
1879 tion canopies with anisotropic scattering, *Journal of Quan-*
1880 *titative Spectroscopy and Radiation Transfer*, 39, 115–129,
1881 1988.

1882 Smolander, S., and P. Stenberg, Simple parameterizations of
1883 the radiation budget of uniform broadleaved and coniferous
1884 canopies, *Remote Sensing of Environment*, 94, 355–363,
1885 2005.

1886 Soler, C., and F. Sillion, Hierarchical instantiation for radios-
1887 ity, in *Rendering Techniques '00*, edited by B. Peroche
1888 and H. Rushmeier, pp. 173–184, Springer Wien, New York,
1889 2000.

1890 Stricker, N. C. M., A. Hahne, D. L. Smith, and J. Delderfield,
1891 ATSR-2: The evolution in its design from ERS-1 to ERS-2,
1892 *ESA Bulletin*, 83, 32–37, 1995.

1893 Thompson, R. L., and N. S. Goel, Two models for rapidly
1894 calculating bidirectional reflectance: Photon spread (ps)
1895 model and statistical photon spread (sps) model, *Remote*
1896 *Sensing Reviews*, 16, 157–207, 1998.

1897 Tian, Y., Y. Wang, Y. Zhang, Y. Knyazikhin, J. Bogaert,
1898 and R. B. Myneni, Radiative transfer based scaling of LAI
1899 retrievals from reflectance data of different resolutions, *Re-*
1900 *remote Sensing of Environment*, 84, 143–159, 2002.

1901 Verhoef, W., Theory of radiative transfer models applied to
1902 optical remote sensing of vegetation canopies, Ph.D. thesis,
1903 Wageningen, 1998.

1904 Verhoef, W., Improved modelling of multiple scattering in leaf
1905 canopies: The model SAIL++, in *Proceedings of the First*
1906 *Symposium on Recent Advances in Quantitative Remote*
1907 *Sensing, Torrent, Spain, September 2002*, edited by A. So-
1908 brino, pp. 11–20, 2002.

1909 Verhoef, W., and H. Bach, Simulation of hyperspectral and
1910 directional radiance images using coupled biophysical and
1911 atmospheric radiative transfer models, *Remote Sensing of*
1912 *Environment*, 87, 23–41, 2003.

1913 Verstraete, M. M., Radiation transfer in plant canopies:
1914 Transmission of direct solar radiation and the role of leaf
1915 orientation, *Journal of Geophysical Research*, 92, 10,985–
1916 10,995, 1987.

1917 Verstraete, M. M., Radiation transfer in plant canopies: Scat-
1918 tering of solar radiation and canopy reflectance, *Journal of*
1919 *Geophysical Research*, 93, 9483–9494, 1988.

- 1920 Weber, J., and J. Penn, Creation and rendering of realistic
1921 trees, in *Proceedings of the 22nd annual conference on*
1922 *Computer graphics and interactive techniques*, pp. 119–
1923 128, ACM press, New York, NY, USA, 1995.
- 1924 Widlowski, J.-L., B. Pinty, N. Gobron, M. M. Verstraete, and
1925 A. B. Davis, Characterization of surface heterogeneity de-
1926 tected at the MISR/TERRA subpixel scale, *Geophysical*
1927 *Research Letters*, 28, 4639–4642, 2001.
- 1928 Widlowski, J.-L., B. Pinty, T. Lavergne, M. M. Verstraete,
1929 and N. Gobron, Using 1-D models to interpret the re-
1930 flectance anisotropy of 3-D canopy targets: Issues and
1931 caveats, *IEEE Transactions on Geoscience and Remote*
1932 *Sensing*, 43, 2008–2017, doi:10.1109/TGRS.2005.853718,
1933 2005.
- 1934 Widlowski, J.-L., T. Lavergne, B. Pinty, M. M. Verstraete,
1935 and N. Gobron, Rayspread: A virtual laboratory for rapid
1936 BRf simulations over 3-D plant canopies, in *Computational*
1937 *Methods in Transport*, edited by G. Frank, pp. 211–231,
1938 ISBN–10 3–540–28,122–3, Lecture Notes in Computational
1939 Science and Engineering Series, 48, Springer Verlag, Berlin,
1940 2006a.
- 1941 Widlowski, J.-L., B. Pinty, T. Lavergne, M. M. Verstraete,
1942 and N. Gobron, Horizontal radiation transport in 3-D for-
1943 est canopies at multiple spatial resolutions: Simulated im-
1944 pact on canopy absorption, *Remote Sensing of Environ-*
1945 *ment*, 103, 379–397, doi:10.1016/j.rse.2006.03.014, 2006b.
-

Table 1. List of the participating models, their RT implementation type, scene construction approach and main scientific reference, as well as the names of their operators during RAMI-3

Model name	RT formalism	Scene Setup	Reference	Participant
<i>1-D models</i>				
ACRM	analytic + MKC	2-layer PP, SD	<i>Kuusk</i> [2001]	Kuusk A. ¹
MBRF	analytic + hotspot kernel	PP, SD	<i>Qin and Xiang</i> [1997]	Qin W. ¹¹
Sail++	N+2 stream	PP, SD	<i>Verhoef</i> [1998, 2002]	Verhoef W. ²
1/2-discret	analytic + DOM	PP, SD	<i>Gobron et al.</i> [1997]	Gobron N. ³
2-Stream	analytic	PP, SD	<i>Pinty et al.</i> [2006]	Lavergne T. ³
<i>3-D models</i>				
5Scale	hybrid (GO)	GP, SD	<i>Leblanc and Chen</i> [2001]	Rochdi N. ⁹ and Leblanc S. ¹²
FLIGHT	MC,RT (forward/reverse)	GP, DL or SD	<i>North</i> [1996]	North P. ¹⁰
4SAIL2	hybrid (4 stream + GO)	2-layer PG,FC	<i>Verhoef and Bach</i> [2003]	Verhoef W. ²
frat	MC,RT (forward)	GP, DL	unpublished	Lewis P. ⁸ and Disney M. ⁸
FRT	hybrid (GO)	GP, SD	<i>Kuusk and Nilson</i> [2000]	Möttus M. ¹ and Kuusk A. ¹
DART	RT (forward) + DOM	voxels, SD	<i>Gastellu-Etcheberry et al.</i> [1996, 2004]	Martin E. ⁵ and Gastellu J-P. ⁵
Drat	MC,RT (reverse)	GP, DL	<i>Lewis</i> [1999]; <i>Saich et al.</i> [2001]	Lewis P. ⁸ and Disney M. ⁸
Hyemalis	radiosity approach	GP, OP, DL	<i>Soler and Sillion</i> [2000], and <i>Helbert et al.</i> [2003]	Ruiloba R. ⁷ , Soler, C. ¹³ , and Bruniquel-Pinel V. ⁷
MAC	hybrid (GO)	GP, SD, FC	<i>Fernandes et al.</i> [2003]	Fernandes R. ⁹ and Rochdi N. ⁹
Rayspread	MC,RT (forward + VR)	GP, DL or SD	<i>Widlowski et al.</i> [2006a]	Lavergne T. ³
raytran	MC,RT (forward)	GP, DL or SD	<i>Govaerts and Verstraete</i> [1998]	Lavergne T. ³
RGM	radiosity	GP, DL	<i>Qin and Gerstl</i> [2000]	Xie D. ⁴
Sprint3	MC,RT (forward + VR)	GP, SD	<i>Thompson and Goel</i> [1998]	Thompson R. ⁶

¹Tartu Observatory, Tõravere

²National Aerospace Laboratory NLR

³Joint Research Centre

⁴School of Geography, Beijing Normal University

⁵Centre d'Etudes Spatiales de la Biosphère

⁶Alachua Research Institute

⁷NOVELTIS, France

⁸Department of Geography, University College London

⁹Canada Centre for Remote Sensing, Ottawa

¹⁰NERC CLASSIC, University of Wales Swansea

¹¹Science Systems and Applications, Inc., Greenbelt, Maryland

¹²Centre Spatial John H. Chapman, Saint-Huber, Québec

¹³ARTIS, INRIA, Rhône-Alpes, France

DL	deterministic location of scatterer
DOM	discrete ordinate method
FC	statistical description of foliage clumping
GO	geometric optics
GP	geometric primitives
MC	Monte Carlo approach
MKC	Markov chain
OP	Optic primitive
PP	plane parallel canopy
PG	parametric description of canopy gaps
RT	ray-tracing scheme
SD	statistical distribution of scatterer
VR	variance reduction technique

Table 2. Model-to-ensemble dispersion statistics, $\bar{\delta}_m$ [%] for six 3-D Monte Carlo models in RAMI-2 and RAMI-3

model name	BRF type	discrete scenes		turbid scenes	
		RAMI-2	RAMI-3	RAMI-2	RAMI-3
DART	ρ_{tot}	-	-	1.42	1.46
	ρ_{co}	-	-	1.80	0.81
	ρ_{mlt}	-	-	21.44	2.72
	ρ_{uc}	-	-	29.02	2.40
drat	ρ_{tot}	1.92	0.55	-	-
	ρ_{co}	15.98	1.43	-	-
	ρ_{mlt}	3.49	1.14	-	-
	ρ_{uc}	72.93	7.47	-	-
FLIGHT	ρ_{tot}	1.26	0.97	9.63	1.06
	ρ_{co}	19.92	3.08	12.72	1.66
	ρ_{mlt}	3.33	2.79	15.40	3.10
	ρ_{uc}	32.99	10.80	14.29	4.48
Rayspread	ρ_{tot}	-	0.55	-	0.64
	ρ_{co}	-	1.42	-	0.69
	ρ_{mlt}	-	1.18	-	1.48
	ρ_{uc}	-	5.88	-	2.62
raytran	ρ_{tot}	1.31	0.60	1.06	0.69
	ρ_{co}	10.24	1.38	1.47	0.78
	ρ_{mlt}	2.73	1.32	10.29	1.81
	ρ_{uc}	32.62	7.20	12.83	3.61
Sprint3	ρ_{tot}	1.29	1.01	9.66	0.69
	ρ_{co}	9.11	2.12	12.67	0.94
	ρ_{mlt}	2.44	1.61	15.27	1.61
	ρ_{uc}	31.53	7.94	15.72	3.44

In each case, the averaging was performed over all available structural, spectral, illumination and viewing conditions.

Table 3. Major variables defining the structural and spectral properties associated to the 100×100 m² “birch stand” scene.

parameter [units]	tree class				
	A	B	C	D	E
tree height [m]	2.5	5.5	8.5	11.5	14.5
LAI/tree [m ² m ⁻²]	0.751	1.081	1.340	1.575	1.805
crown height [m]	1.237	2.952	4.919	7.137	9.606
crown width [m]	0.611	0.995	1.430	1.937	2.538
trunk height [m]	1.263	2.548	3.581	4.363	4.894
trunk width [m]	0.014	0.033	0.054	0.078	0.107
tree density [stem/ha]	38	507	981	261	13
red leaf reflectance	0.10	0.09	0.08	0.07	0.06
red leaf transmittance	0.06	0.05	0.04	0.03	0.03
red trunk reflectance	0.32	0.31	0.30	0.29	0.28
NIR leaf reflectance	0.49	0.48	0.47	0.46	0.45
NIR leaf transmittance	0.50	0.49	0.48	0.47	0.46
NIR trunk reflectance	0.40	0.39	0.38	0.37	0.36

The reflectance of the Lambertian soil was 0.127 (0.159) in the red (NIR) spectral band. The scattering properties of both leaves and trunks were Lambertian.

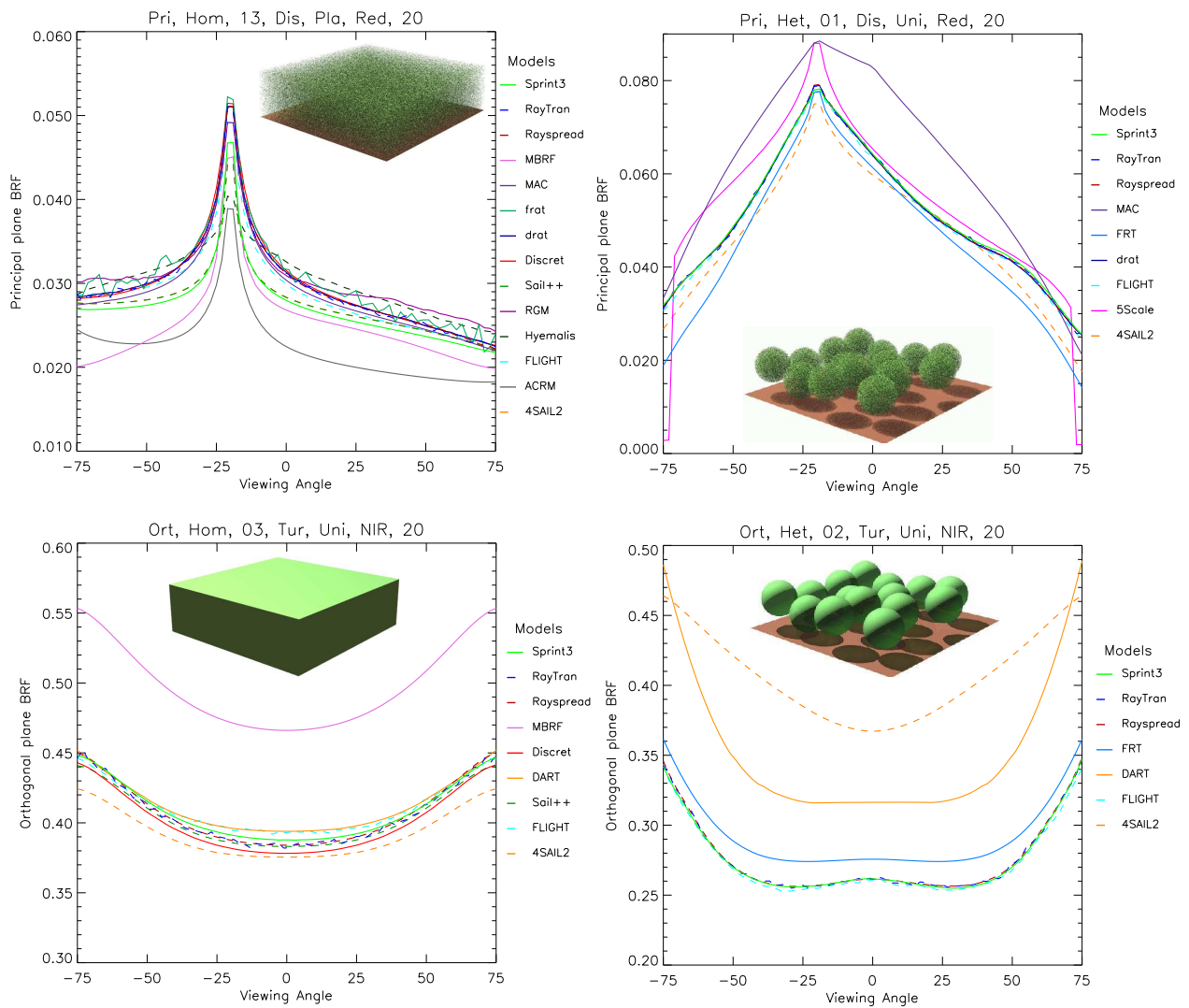


Figure 1. Sample BRF results for structurally homogeneous (left panels) and "floating spheres" (right panels) canopies. Model simulations along the principal plane (top panels) relate to test cases with finite-sized scatterers and spectral properties that are typical of the red spectral band. Those along the orthogonal plane (bottom panels) relate to turbid medium foliage representations with spectral properties that are typical of the near-infrared (NIR). The illumination zenith angle was 20° in all cases. Also shown are graphical representations of the various canopy structures.

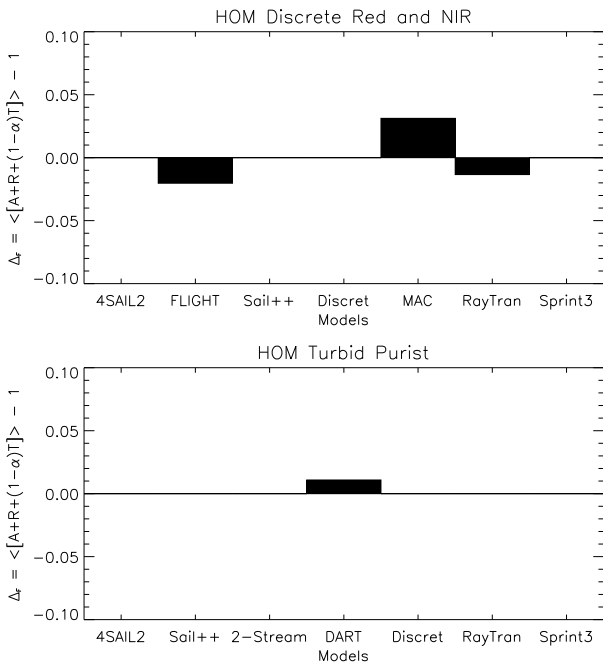


Figure 2. The average deviation from energy conservation (Δ_F) for RT models performing 1) the discrete homogeneous baseline scenarios in the solar domain (top panel), and 2) the turbid medium homogeneous test cases under conservative scattering conditions (bottom panel).

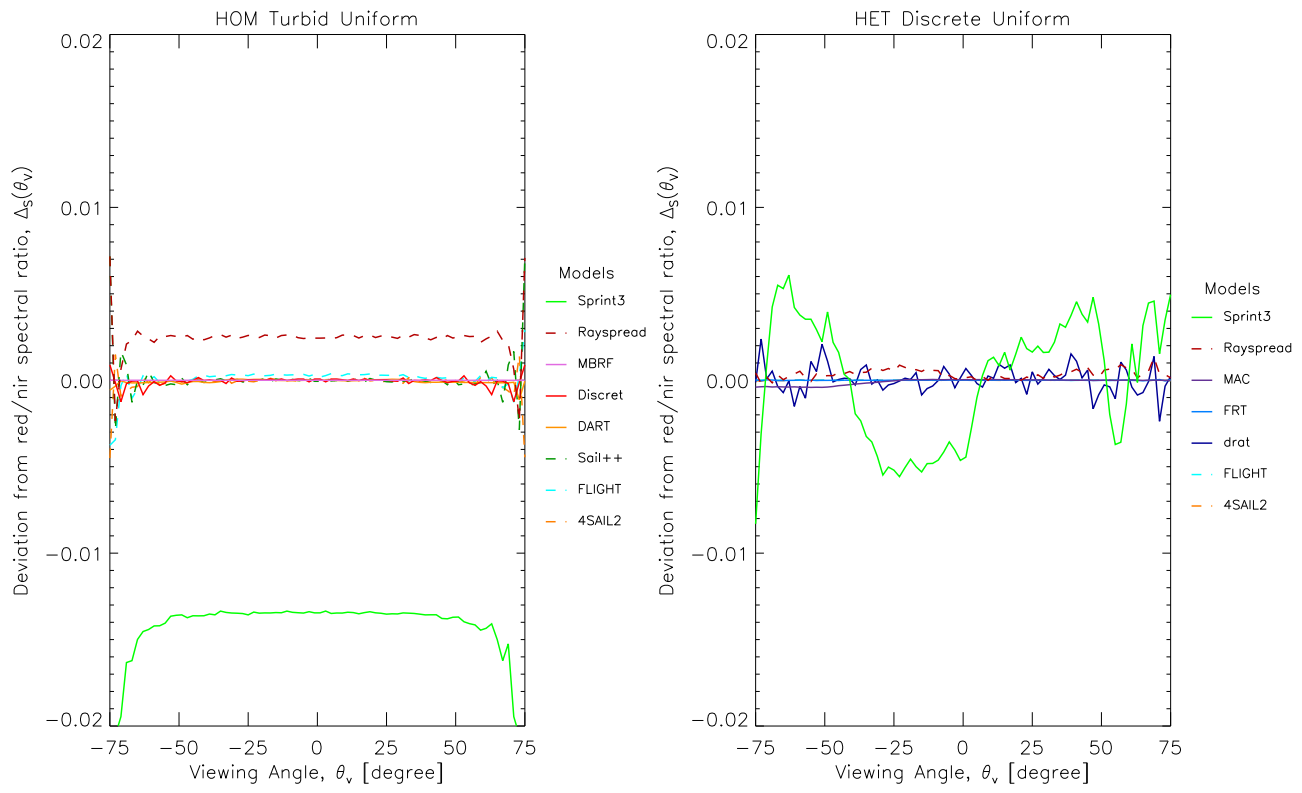


Figure 3. Average deviation from the true spectral ratio of the single-uncollided BRDF components in the red and NIR spectral domains, Δ_S , as a function of view zenith angle for homogeneous turbid medium canopies (left) and discrete floating-spheres canopies (right) with uniform LNDs.

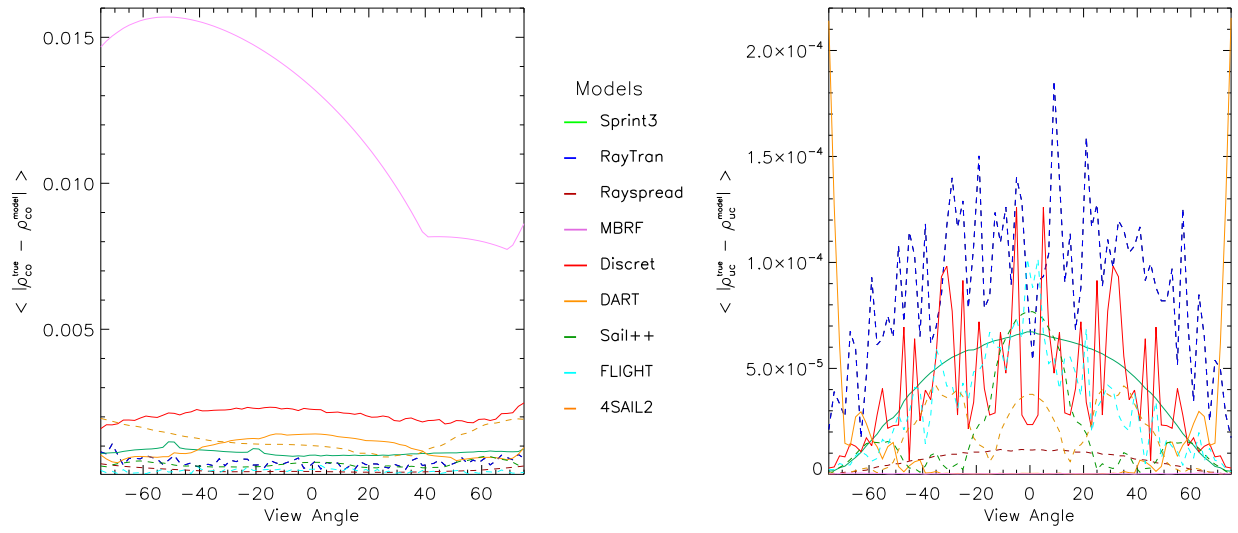


Figure 4. The mean absolute error between model simulations and the analytical formulation of the single-collided, ρ_{co} (left panel) and the single-uncollided, ρ_{uc} (right panel) BRF components of a homogeneous turbid medium canopy with uniform LND and Lambertian scattering laws. For any view zenith angle the averaging was performed over the principal and orthogonal plane, as well as, for illumination zenith angles of 20° and 50° .

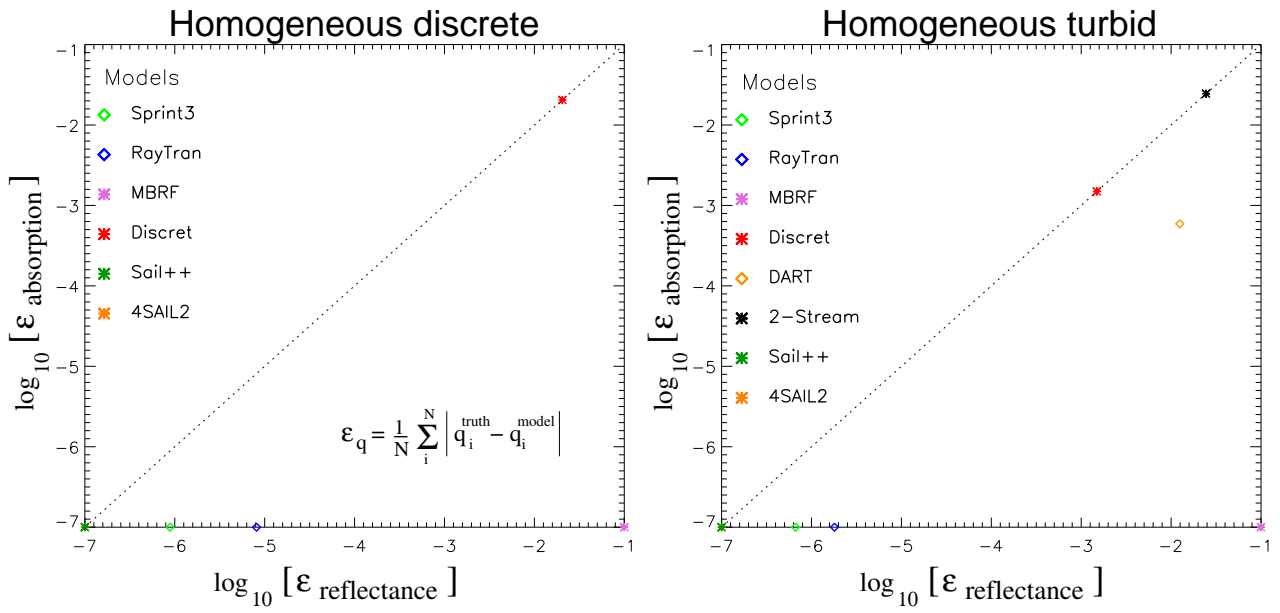


Figure 5. The average absolute deviation, ε_q between RT model estimates and the true canopy absorption, $q^{\text{truth}} = A = 0$ (y-axis) or reflectance $q^{\text{truth}} = R = 1$ (x-axis), on a logarithmic scale, for structurally homogeneous canopies with finite-sized (left panel) and turbid medium (right panel) foliage representations under conservative scattering conditions. The averaging was performed over ($N = 18$) test cases with varying LAI, LND and θ_i . Note that—with the exception of MBRF which did not provide absorption estimates—all exact A and R values are plotted at $\log \varepsilon_q = -7$.

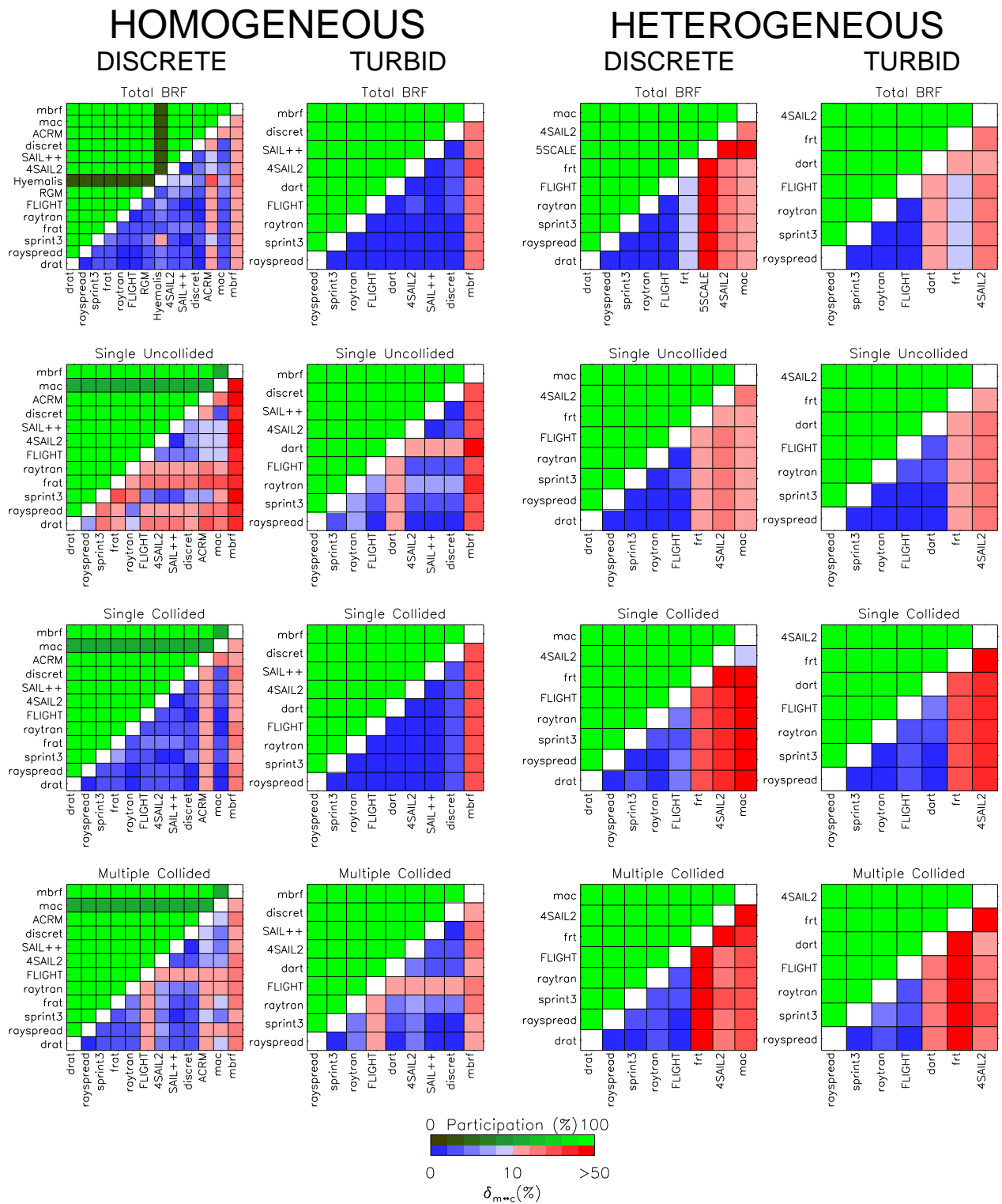


Figure 6. Model-to-model differences $\delta_{m \leftrightarrow c}$ of the total (top row), single-uncollided (second row), single-collided (third row) and multiple-collided (last row) BRF data of models performing the required simulations for structurally homogeneous canopies with finite-sized (leftmost column) and turbid medium (middle-left column) foliage representations, as well as, for “floating spheres” scenarios with finite-sized (middle-right column) and turbid medium (rightmost column) foliage representations in the solar domain. The lower right half of every panel indicates $\delta_{m \leftrightarrow c}$ in [%] (blue-red colour scheme), whereas the top left half indicates the percentage of available test cases that pairs of models performed together (black-green colour scheme). The green colour scale increments in steps of 10%, the blue in steps of 2% (up to $\delta_{m \leftrightarrow c} = 10\%$), and the red in steps of 10% (with a bright red colour indicating $\delta_{m \leftrightarrow c} > 50\%$).

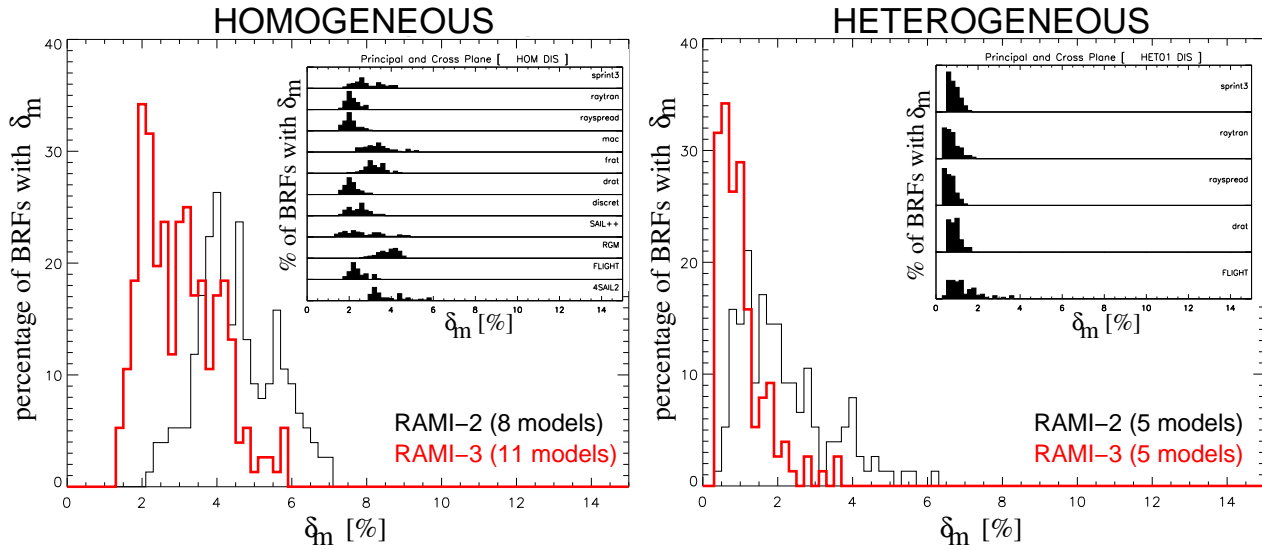


Figure 7. The inlaid panels show histograms of model-to-ensemble differences, δ_m [%] for selected models participating in the discrete homogeneous (left panel) and discrete “floating spheres” (right panel) test cases. Included in the generation of these histograms are BRF simulations in the principal and orthogonal planes using illumination zenith angles of 20° and 50° in both the red and NIR spectral domain. The main panels show the envelope encompassing the various RAMI-3 (red colour) histograms—shown in the inlaid graphs—in relation to that obtained during RAMI-2 (black line) for the same set of test cases.

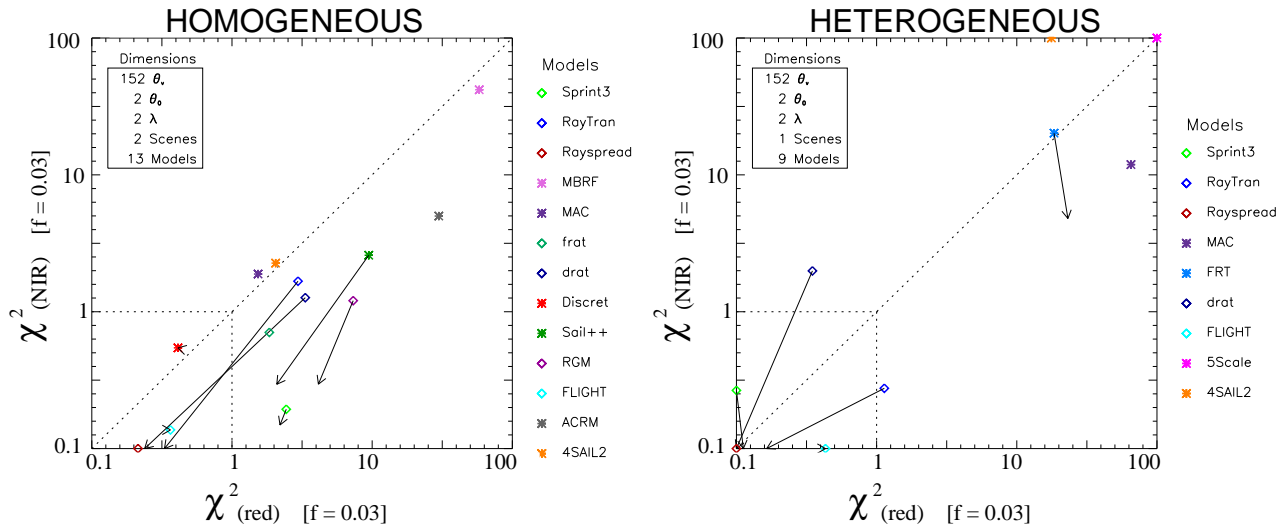


Figure 8. χ^2 statistics in the red (X-axis) and NIR (Y-axis) wavelengths for the structurally homogeneous (left panel) and the “floating spheres” (right panel) baseline scenarios with finite sized scatterers. Arrows indicate changes in the χ^2 values of models performing both in RAMI-2 (base of arrow) and in RAMI-3 (tip of arrow) using the letter $\bar{\rho}_{3D}$ as reference.

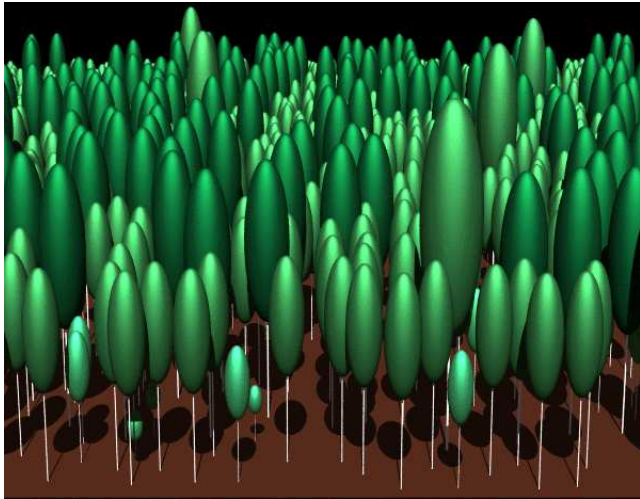


Figure 9. Graphical representation of a portion of the RAMI-3 “birch stand” scene when looking from its southern edge in an northward direction towards the centre of the scene. The sun is assumed to be located behind the viewer, *i.e.*, “south” of the scene.

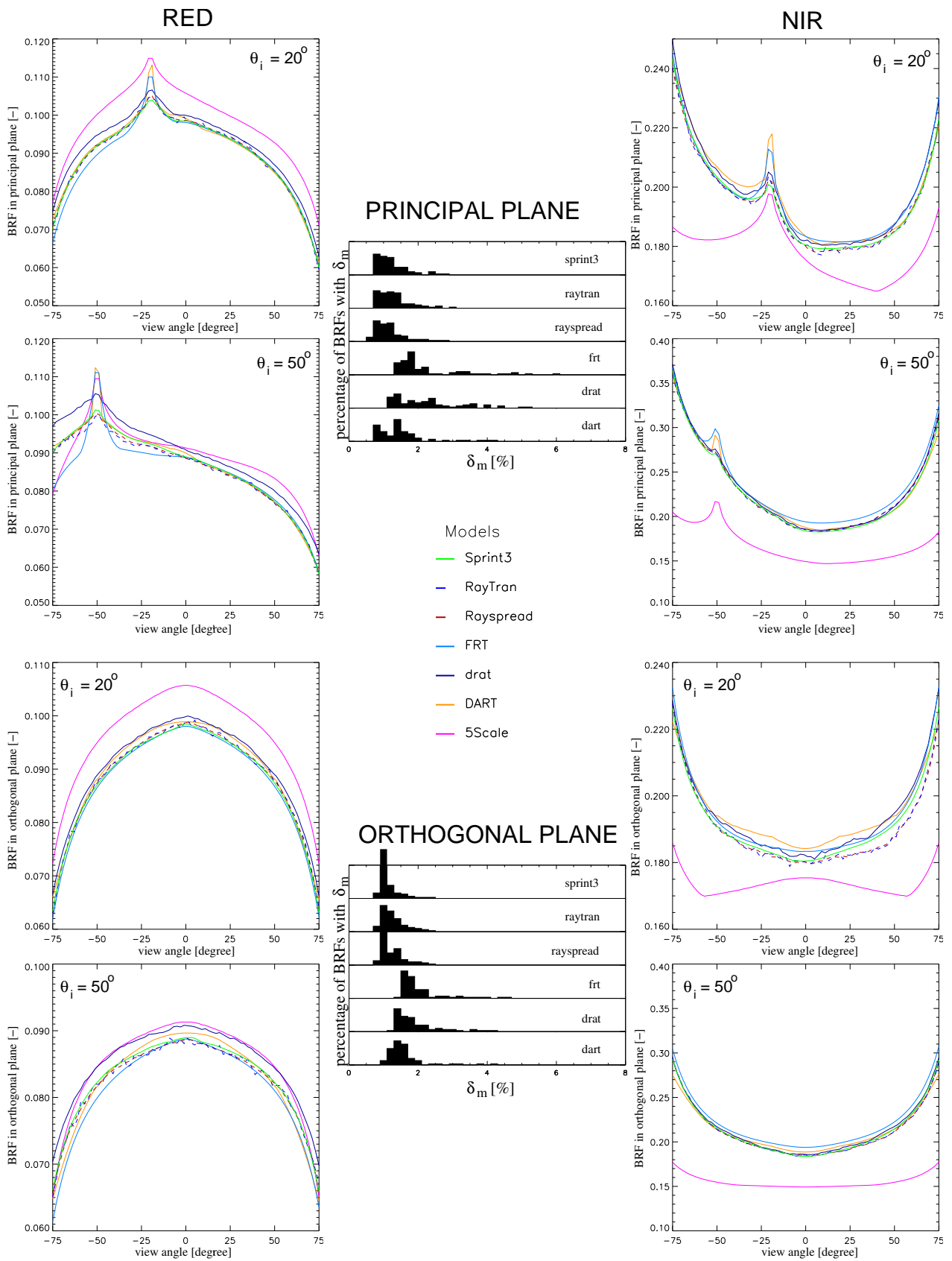


Figure 10. Model simulated BRFs in the red (left column) and NIR (right column) spectral domain of the “birch stand” along the principal (upper panels) and orthogonal (lower panels) planes under illumination conditions of $\theta_i = 20^\circ$ and $\theta_i = 50^\circ$. Histograms of model-to-ensemble deviations δ_m are provided for (all models but 5Scale in) both observational planes (central panels).

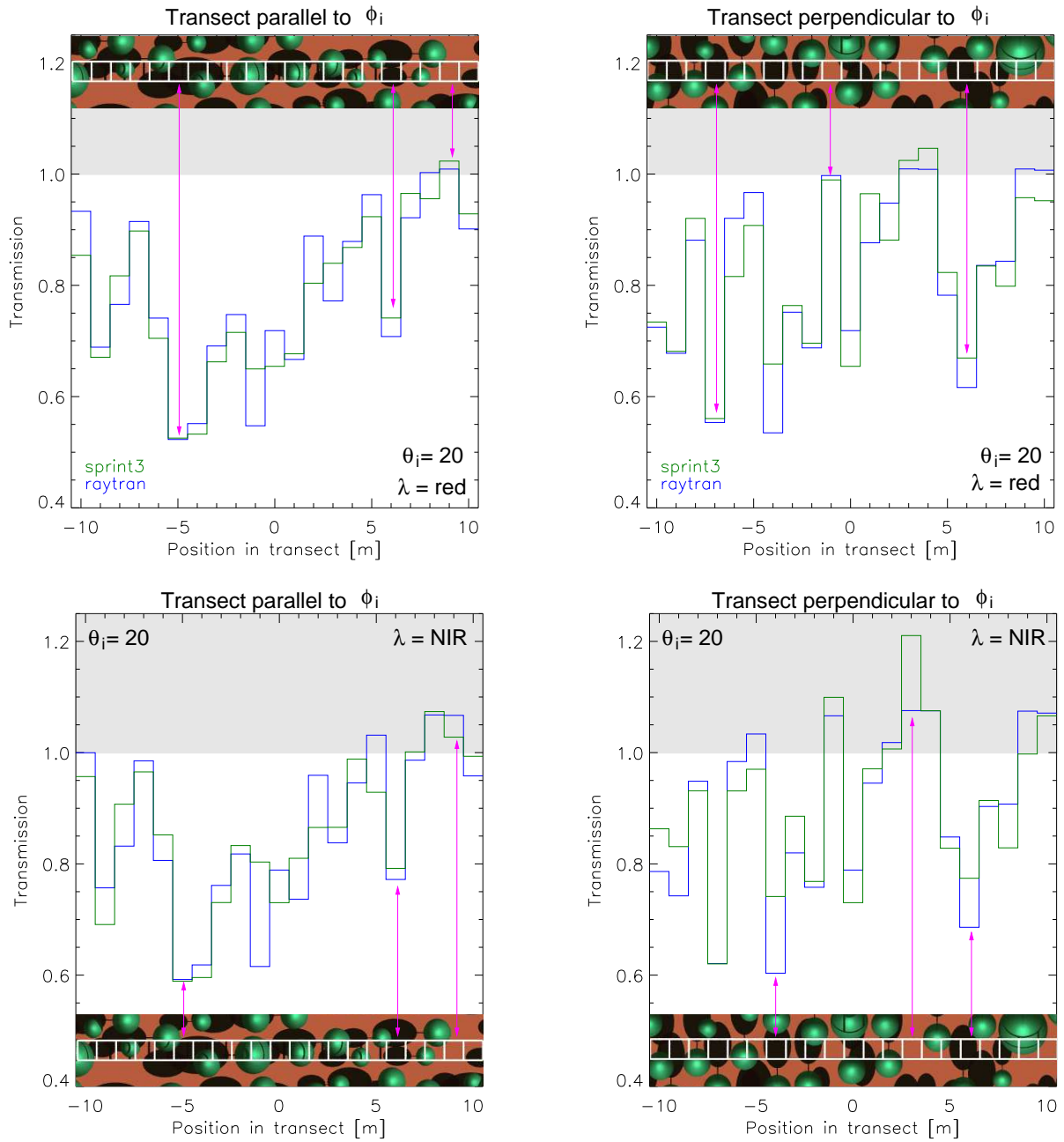


Figure 11. Model simulated local transmissions along transects composed of 21 adjacent $1 \times 1 \text{ m}^2$ patches oriented parallel (left panels) and perpendicular (right panels) to the direction of the illumination azimuth (ϕ_i) in the red (top panels) and NIR (bottom panels) spectral domain. Pink arrows indicate obvious correlations with predominantly shadowed and illuminated patches in the various graphical representations of the transects (in-laid images featuring the transect as a sequence of white squares). Transmission values that are larger than unity fall within the grey shaded area.

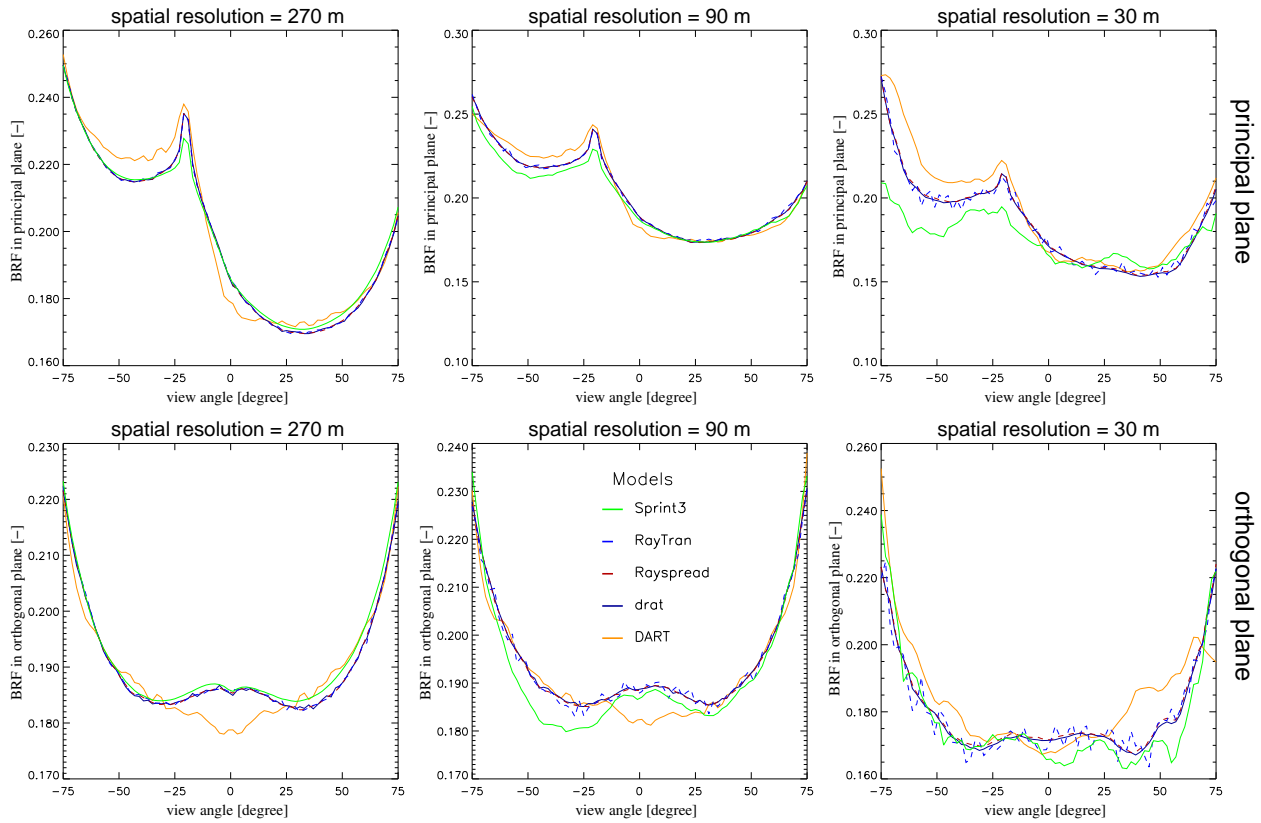


Figure 12. Model simulated BRFs along the principal (top panels) and orthogonal (bottom panels) planes of the “true zoom-in” scene at spatial resolutions of 270 m (left), 90 m (middle) and 30 m (right). The illumination zenith angle was set to 20° and the spectral properties are typical for the NIR spectral domain.

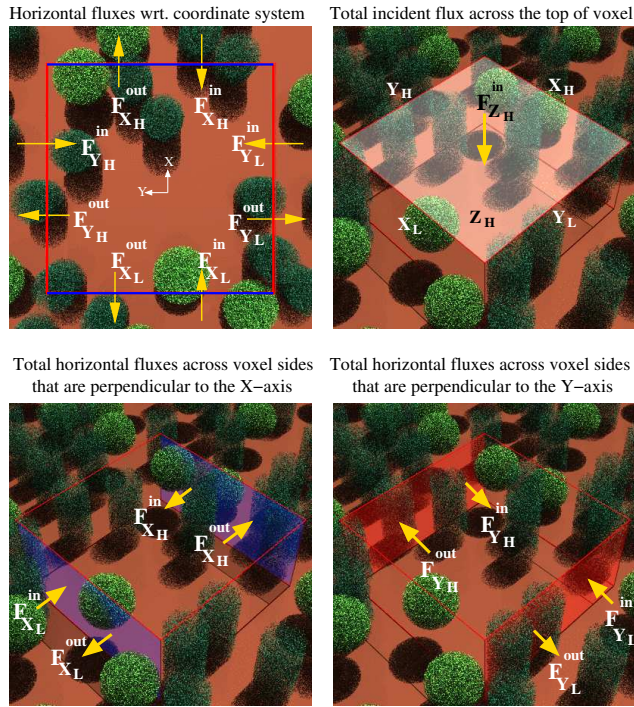


Figure 13. Schematics of the various horizontal (and incident) total fluxes entering and exiting a voxel—here of $30 \times 30 \times 15$ m lateral dimensions—via its lateral (and top) sides. Note that the X-axis is aligned with the azimuthal direction of the incident light.

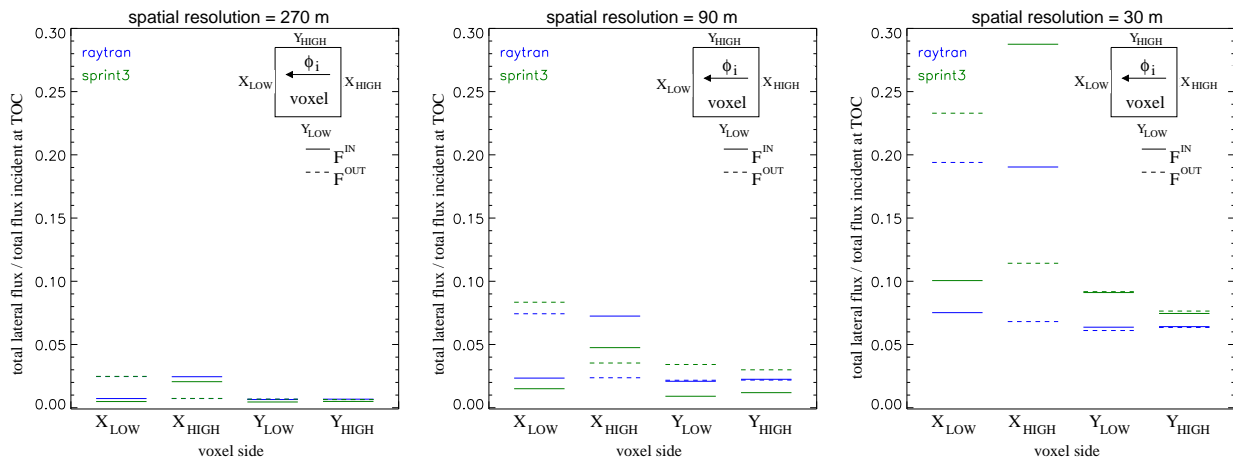


Figure 14. Normalised horizontal fluxes entering (solid) and exiting (dashed) the lateral sides of voxels with spatial dimensions equal to 270 m (left), 90 m (middle) and 30 m (right) in the NIR spectral domain. The voxels are centered at the origin of the local coordinate system and have a height of 15 m. The illumination azimuth, ϕ_i is parallel (perpendicular) to the voxel sides labeled Y_{LOW} and Y_{HIGH} (X_{LOW} and X_{HIGH}), and $\theta_i = 20^\circ$.

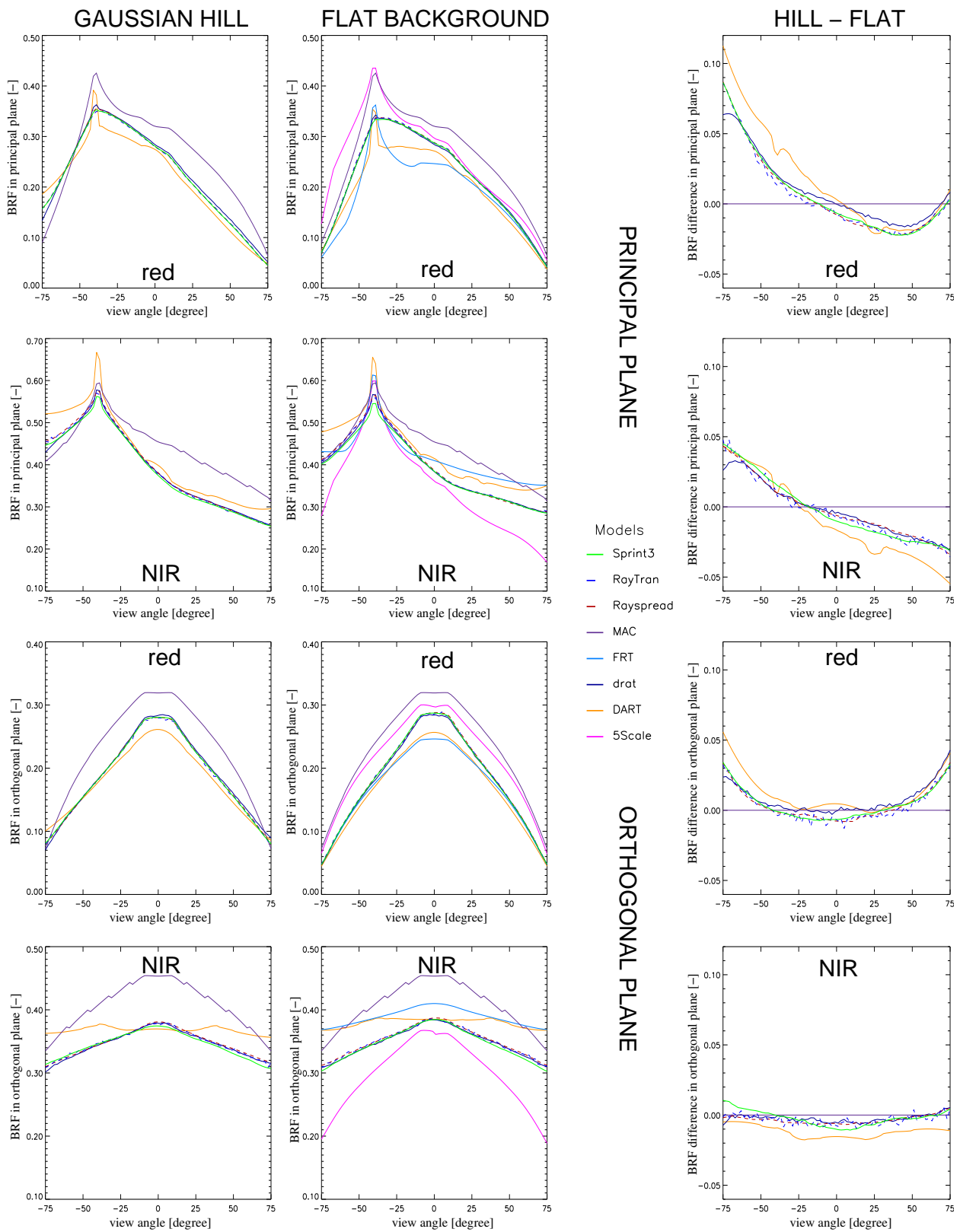


Figure 15. Model simulated BRFs in the principal (top 2 rows) and orthogonal (bottom 2 rows) viewing planes for the “conifer forest” scene with topography (left panels), without topography (middle panels), as well as, the difference between these two, respectively (right panels). Simulations pertain to the red (top and third row) and near-infrared (second and bottom row) spectral regimes at $\theta_i = 40^\circ$.

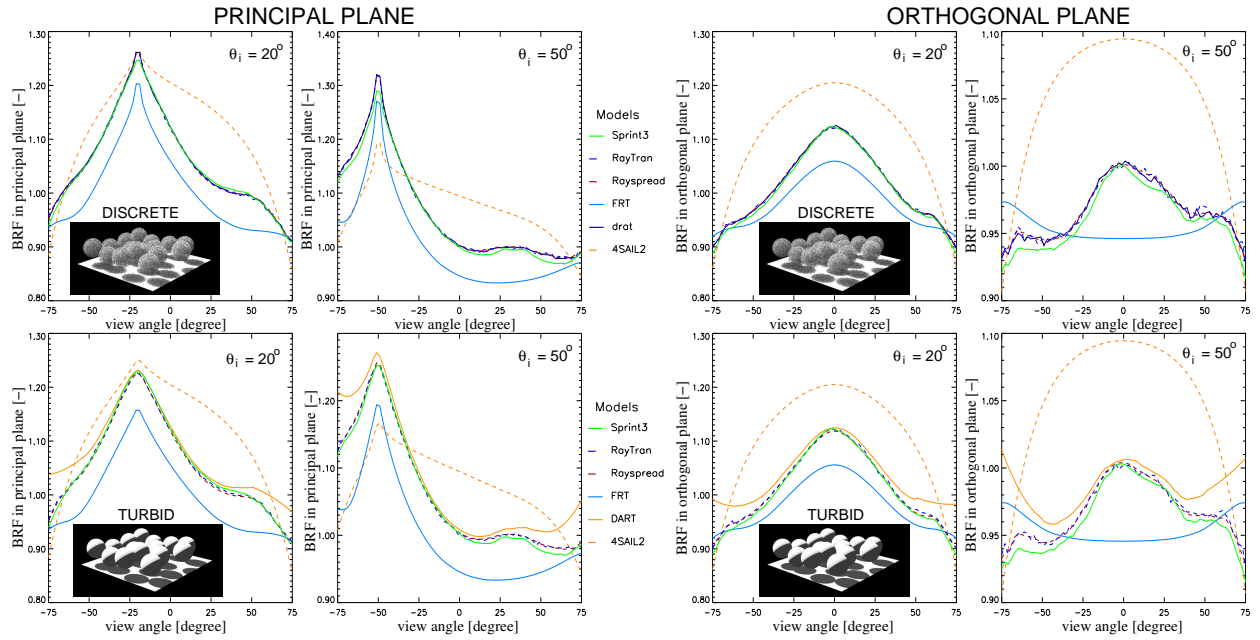


Figure 16. Model simulated BRFs for the “floating spheres” scene under conservative scattering conditions (purist corner). Results are shown in the principal (left columns) and orthogonal (right columns) observation planes for discrete (top row) and turbid medium (bottom row) foliage representations and two different illumination zenith angles (θ_i). The structure of the scenes is indicated in the inlaid images.

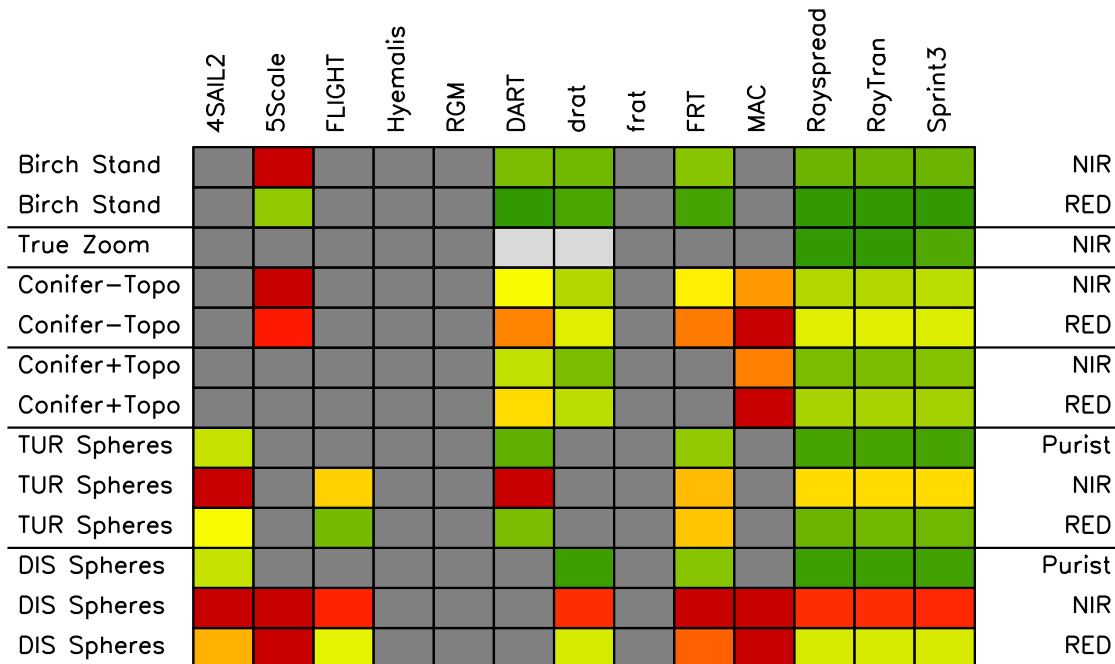
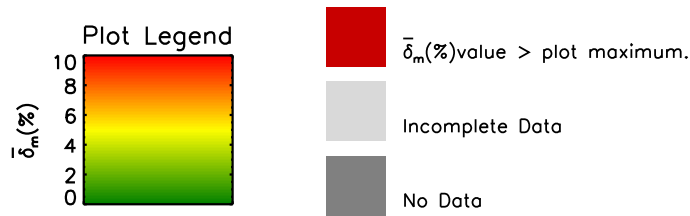
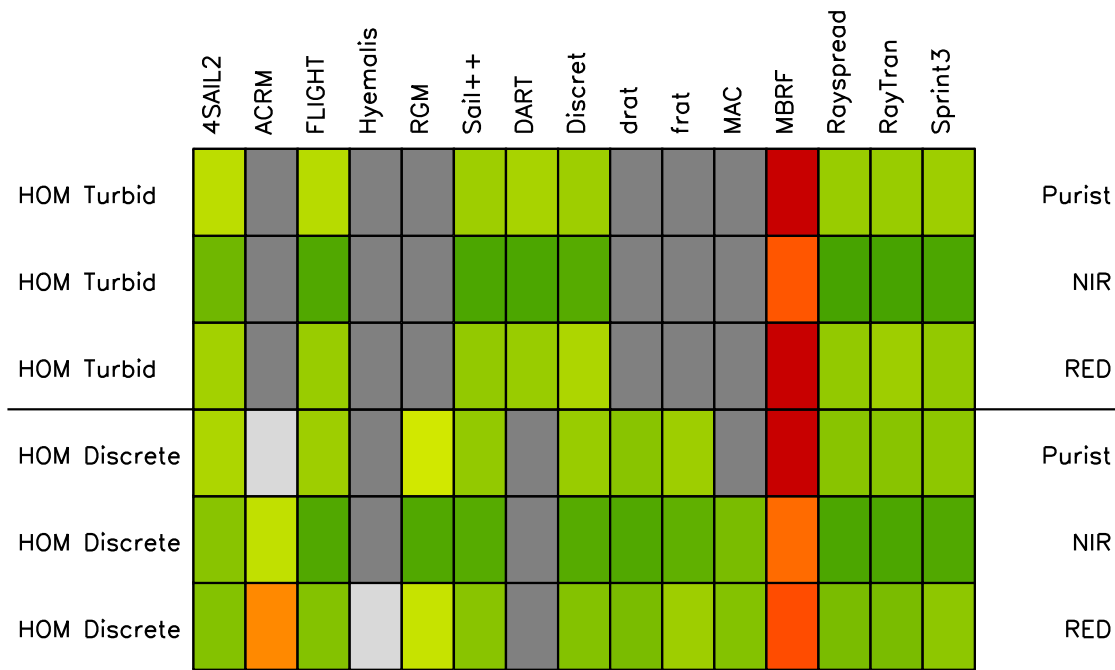


Figure 17. Model performance and participation during RAMI-3 for structurally homogeneous (top table) and heterogeneous (bottom table) discrete canopy representation. Model names are listed on the top of each table (one per column). The experiment identifier is provided to the left, the spectral regime to the right, of each table column. Light (dark) grey fields indicate incomplete (no) data submission. The green-yellow-red colour scheme represent the integrated model-to-ensemble difference, $\bar{\delta}$ [%] obtained with respect to all models that have performed the complete set of prescribed total BRF simulations for any given experiment/spectral regime combination.